



## *Arabidopsis thaliana* serine hydroxymethyltransferases: functions, structures, and perspectives

Isabel Nogués<sup>a</sup>, Bartosz Sekula<sup>b,c</sup>, Sebastiana Angelaccio<sup>d</sup>, Marta Grzechowiak<sup>e</sup>, Angela Tramonti<sup>f</sup>, Roberto Contestabile<sup>d</sup>, Milosz Ruskowski<sup>b,e,\*</sup>

<sup>a</sup> Research Institute on Terrestrial Ecosystems, Italian National Research Council, Monterotondo Scalo, Rome, Italy

<sup>b</sup> Synchrotron Radiation Research Section of MCL, National Cancer Institute, Argonne, IL, USA

<sup>c</sup> Institute of Molecular and Industrial Biotechnology, Lodz University of Technology, Lodz, Poland

<sup>d</sup> Department of Biochemical Sciences "A. Rossi Fanelli", Sapienza University of Rome, Laboratory Affiliated to Istituto Pasteur Italia-Fondazione Cenci Bolognetti, P. le Aldo Moro 5, 00185, Rome, Italy

<sup>e</sup> Department of Structural Biology of Eukaryotes, Institute of Bioorganic Chemistry, Polish Academy of Sciences, Poznan, Poland

<sup>f</sup> Institute of Molecular Biology and Pathology, National Research Council, Rome, Italy

### ABSTRACT

Serine hydroxymethyltransferase (SHM) is one of the hallmarks of one-carbon metabolism. In plants, isoforms of SHM participate in photorespiration and/or transfer the one-carbon unit from L-serine to tetrahydrofolate (THF), hence producing 5,10-CH<sub>2</sub>-THF that is needed, e.g., for biosynthesis of methionine, thymidylate, and purines. These links highlight the importance of SHM activity in DNA biogenesis, its epigenetic methylations, and in stress responses. Plant genomes encode several SHM isoforms that localize to cytosol, mitochondria, plastids, and nucleus. In this work, we present a thorough functional and structural characterization of all seven SHM isoforms from *Arabidopsis thaliana* (AtSHM1-7). In particular, we analyzed tissue-specific expression profiles of the AtSHM genes. We also compared catalytic properties of the active AtSHM1-4 in terms of catalytic efficiency in both directions and inhibition by the THF substrate. Despite numerous attempts to rescue the SHM activity of AtSHM5-7, we failed, which points towards different physiological functions of these isoforms. Comparative analysis of experimental and predicted three-dimensional structures of AtSHM1-7 proteins indicated differences in regions that surround the entrance to the active site cavity.

### 1. Introduction

Serine hydroxymethyltransferase (SHM, EC 2.1.2.1) is a pyridoxal 5'-phosphate (PLP)-dependent enzyme with a central role in one-carbon folate metabolism. Although the enzyme has multiple catalytic activities, its main function is to catalyze the reversible conversion of L-serine and tetrahydrofolate (THF or tetrahydropteroylglutamate; H<sub>4</sub>PteGlu) to glycine and 5,10-methylenetetrahydrofolate (5,10-CH<sub>2</sub>-THF). The Ser → Gly reaction supplies one-carbon units for a series of vital biosynthetic processes, such as the synthesis of methionine, thymidylate, and purines, underlying its importance in DNA biogenesis and cellular methylation reactions (Schirch, 1982; Matthews and Drummond, 1990; Schirch and Szebenyi, 2005). In plants, however, SHM reaction in the other direction (Gly → Ser) is also indispensable, being an integral step of the photorespiratory pathway (Timm and Hagemann, 2020).

SHM is structurally conserved and ubiquitous in nature; many sequences from Eukarya, Eubacteria, and Archaea are available in databases, and several crystal structures have been solved. In Eubacteria and Archaea, single genes encode the SHM enzymes, which exhibit a

homodimeric structure. In animals and fungi, two genes encode two SHM isoforms (cytosolic and mitochondrial) that form tetramers (Martini et al., 1987, 1989; Garrow et al., 1993; Kastanos et al., 1997; Renwick et al., 1998). In plants, the situation is much more complicated due to a high number of SHM isoforms, e.g., seven in *Arabidopsis thaliana* (At) (Hanson and Roje, 2001; Zhang et al., 2010), seven in *Medicago truncatula* (Ruskowski et al., 2018), five in *Oryza sativa* (Mishra et al., 2019), and at least twelve in *Glycine max* (Lakhssassi et al., 2019). The multiple isoforms of plant SHMs are distributed among cellular compartments. For instance, *A. thaliana* SHM isoforms localize to mitochondria (AtSHM1, AtSHM2), chloroplast (AtSHM3), cytosol (AtSHM4, AtSHM5), and nucleus (AtSHM6, AtSHM7) (Zhang et al., 2010; Wei et al., 2013; Huang et al., 2016; Ruskowski et al., 2018). The existence of so many isoforms is probably related to the plants' need for metabolic flexibility and reprogramming in response to changing environmental conditions (Hodges, 2002). Interestingly, at least some SHM isoforms (AtSHM1 and AtSHM4) are controlled by the circadian clock (McClung et al., 2000).

Plant SHM isoforms play an important role in the photorespiration

\* Corresponding author. Department of Structural Biology of Eukaryotes, Institute of Bioorganic Chemistry, Polish Academy of Sciences, Poznan, Poland.  
E-mail address: [mruskowski@ibch.poznan.pl](mailto:mruskowski@ibch.poznan.pl) (M. Ruskowski).

<https://doi.org/10.1016/j.plaphy.2022.07.025>

Received 1 June 2022; Received in revised form 12 July 2022; Accepted 20 July 2022

Available online 31 July 2022

0981-9428/© 2022 The Author(s). Published by Elsevier Masson SAS. This is an open access article under the CC BY license (<http://creativecommons.org/licenses/by/4.0/>).

pathway and the resistance to environmental stresses (Fang et al., 2020b). Indeed, it has been found that a mitochondrial *SHM* gene mutation in rice (*osshm1*) obstructs the photorespiration pathway, resulting in the accumulation of reactive oxygen species (ROS) (Wang et al., 2015). Also, in *A. thaliana*, the *shm1-1* mutant (in the gene encoding the mitochondrial *AtSHM1* isoform) has the conditional lethal photorespiratory phenotype (Somerville and Ogren, 1981; Moreno et al., 2005; Voll et al., 2006). The involvement of SHM in plant stress tolerance has been assessed in several studies. *A. thaliana shm1-1* mutants are more susceptible to infection by biotrophic and necrotrophic plant pathogens. These mutants also accumulate more H<sub>2</sub>O<sub>2</sub> than wild-type plants under salt stress (Moreno et al., 2005). On the other hand, the *Oryza sativa* transgenic line *Lsi1-OX*, in which *OsSHM* is up-regulated, presented an enhanced chilling tolerance and lower ROS levels; *OsSHM* localizes to the endoplasmic reticulum (Fang et al., 2020a). Moreover, computational and genetic investigations suggested that *AtSHM5*, *AtSHM6*, and *AtSHM7* are involved in the development and maturation of fruit (Zhang et al., 2017) and in gametogenesis (Pagnussat et al., 2005). These results suggest important regulatory functions of some *AtSHM*, perhaps similar to the RNA binding capability of the human cytosolic (*HsSHMT1*) (Guiducci et al., 2019). However, the underlying molecular mechanisms in plants remain to be determined.

*In vitro* SHM activity has been reported for *A. thaliana* mitochondrial, cytosolic, and plastidic isoforms (*AtSHM1*, *AtSHM2*, *AtSHM3*, *AtSHM4*), but no functional information is available for *AtSHM5*, *AtSHM6*, or *AtSHM7*. Wei et al. (2013) characterized *AtSHM1*, *AtSHM2*, and *AtSHM4* concerning the impact of folate polyglutamylation on substrate saturation kinetics. The authors found that only *AtSHM1* and *AtSHM2* had increased turnover rates at high enzyme concentrations in the presence of monoglutamylated folates but not with pentaglutamylated folate substrates. Such differences in catalytic efficiency of *AtSHMs* may be an adaptation to different folate concentrations in subcellular compartments. In another study, plastidic *AtSHM3* was characterized by Zhang et al. (2010). The authors revealed an increase in the substrate affinity and the catalytic efficiency for H<sub>4</sub>PteGlu<sub>n</sub> with *n* (1–8). *AtSHM3* is also subjected to H<sub>4</sub>PteGlu<sub>1–8</sub> substrate inhibition and inhibition by 5-methyl-H<sub>4</sub>PteGlu<sub>n</sub> and 5-formyl-H<sub>4</sub>PteGlu<sub>n</sub> (*n* = 1 or 5); pentaglutamylated inhibitors are more effective. However, the authors calculated that these molecules should not impact *AtSHM3* activity under the folate concentration estimated for plastids. Regarding *AtSHM2* (mitochondrial) and *AtSHM4* (cytosolic), their interaction with antifolates has been assayed by us from the structural and kinetic perspective (Ruszkowski et al., 2019). Although the *AtSHM5* isoform was expressed, the purified protein was catalytically inactive (Wei et al., 2013). The nuclear *AtSHM7* has also been shown to lack SHM activity *in vitro* (Huang et al., 2016). The authors suggested a novel function for this isoform in regulating *S*-adenosylmethionine (SAM) biosynthesis and epigenetic maintenance of sulfur homeostasis via DNA methylation (Huang et al., 2016). Until now, there has been no experimental evidence of whether *AtSHM6* has SHM activity, although as *AtSHM7*, it holds a nuclear-targeting signal peptide (Zhang et al., 2010).

Considering the link between plant mitochondrial SHM isoforms with the maintenance of redox homeostasis during photorespiration, it is not surprising that the organellar SHM isoforms have received more attention than the cytosolic isoforms. Here we focus on analyzing gene expression, kinetic characterization, and structural comparison of all seven *AtSHM* isoforms, whose possible functions are still poorly understood.

## 2. Material and methods

### 2.1. Cloning of *A. thaliana SHMs*

*AtSHMs* were produced using the protocol described for *AtSHM2* and *AtSHM4* (Ruszkowski et al., 2019). Briefly, RNA isolated from *A. thaliana* leaves using the RNeasy Plant Mini Kit (Qiagen) was

reverse-transcribed into the complementary DNA (cDNA) with SuperScript II reverse transcriptase (Life Technologies). The open reading frames coding for *AtSHM*(1–7) were amplified by polymerase chain reaction. Except for the cytosolic *AtSHM4&5*, N-terminal signal peptides were truncated in the construct design to yield *AtSHM1*-Nt46 (meaning that the residue 46 in the genuine sequence is the first one in the construct), *AtSHM2*-Nt46, *AtSHM3*-Nt76, *AtSHM6*-Nt127, and *AtSHM7*-Nt123. Prediction of the mature SHM sequences was based on a hybrid approach using TargetP 1.1 (Emanuelsson et al., 2000) prediction, refined by comparison of homologous sequences from other plant species and prediction of disordered regions. The complete list of primers is provided in Supplementary Table 1. Expression plasmids, based on the pMCSG68 vector (Midwest Center for Structural Genomics, USA), were created by the ligase-independent cloning method (Kim et al., 2011). The plasmids were used to transform *E. coli* BL21(DE3) Gold competent cells for protein expression. These procedures allowed the expression of *AtSHMs* with a cleavable N-terminal His<sub>6</sub>-tag. The correctness of the coding sequences was verified by DNA sequencing.

### 2.2. Heterologous expression and purification of *A. thaliana SHMs*

An overnight culture (40 mL) of BL21(DE3) cells, transformed with the corresponding plasmid, was inoculated into 2 L of lysogeny broth containing 100 µg/mL ampicillin. Bacteria were grown aerobically at 37 °C to the exponential phase (until the optical density at 600 nm was 1.0). Then, the temperature was reduced to 4 °C, and after shaking for 1 h, the temperature was changed to 18 °C, and isopropyl-D-thiogalactopyranoside was added at a final concentration of 0.5 mM to induce protein expression. Bacteria were harvested after 18 h and suspended in 35 mL of binding buffer (50 mM Hepes-NaOH pH 7.5; 500 mM NaCl; 20 mM imidazole, 0.2 mM DTT) and stored at –20 °C. Cell lysis was carried out by sonication at 70% amplitude using PULSE protocol, 4 s ON/26 s OFF, and the lysates were cleared by centrifugation at 11,000 g for 20 min. The supernatant was applied onto a Ni-NTA column equilibrated with the binding buffer. The column was washed with the equilibration buffer until the absorbance at 260 nm was below 0.1, and then with the same buffer with 400 mM imidazole. Fractions were collected, and those absorbing at 422 nm (for samples that did absorb at 422 nm) were pooled; absorption at 422 nm indicates bound PLP and in our experience corresponds to purest samples. The samples were dialyzed against 20 mM potassium phosphate at pH 7.2, containing 300 mM NaCl, 0.2 mM DTT. The purity of each *AtSHMs* sample was checked by SDS-PAGE. The concentration of catalytically active *AtSHMs* was calculated by determining the amount of bound PLP. After the addition of NaOH (0.2 N final concentration) to the enzyme solution, the absorbance at 388 nm was measured. The released PLP has an extinction coefficient of 6550 M<sup>-1</sup> (Peterson and Sober, 1954).

For structural studies, His<sub>6</sub>-tag was cleaved with the TEV (tobacco etch virus) protease after the first affinity chromatography step. Afterward, the imidazole concentration was lowered to 20 mM by dialysis, and the sample was run through the Ni-NTA resin again. The flow-through was collected, concentrated to 2 mL volume, and subjected to size-exclusion chromatography using Superdex200 16/60 column equilibrated in 25 mM Hepes-NaOH pH 7.5; 50 mM NaCl; 100 mM KCl; 1 mM Tris(2-carboxyethyl)phosphine hydrochloride.

### 2.3. THF-dependent activity

THF, 5,10-CH<sub>2</sub>-THF and 5-formyl-THF were kindly provided by Merck & Cie (Schaffhausen, Switzerland). All experiments were performed in triplicates (three measurements on the same enzyme preparations) using a Hewlett-Packard 8453 diode-array spectrophotometer (Agilent Technologies, Santa Clara, CA).

#### 2.4. SHM reaction with L-serine and THF as substrates

Measurements of the initial velocity of the serine + THF → glycine + 5,10-CH<sub>2</sub>-THF (Ser → Gly) reaction were carried out with 0.2 μM enzyme samples with L-serine and THF as substrates by means of a spectrophotometric coupled assay, in which the 5,10-CH<sub>2</sub>-THF produced by the SHM reaction was oxidized by the NADP<sup>+</sup>-dependent *E. coli* 5,10-methylenetetrahydrofolate dehydrogenase (Angelaccio et al., 2014). Assays were carried out at two different pH values (7.0 and 8.0) at 30 °C. Saturation curves were obtained with AtSHMs, keeping one substrate at a fixed concentration while varying the concentration of the other substrate. Kinetic parameters were determined using Equation (1) when L-serine was the fixed substrate or the Michaelis–Menten equation when THF was the fixed substrate.

Equation 1

$$V_i = V_{\max} \frac{[THF]}{[THF] + K_m THF \left(1 + \frac{[THF]}{K_i}\right)} \quad (1)$$

where  $V_i$  stands for the initial velocity,  $V_{\max}$  is the maximum velocity,  $[THF]$  is the concentration of the variable substrate,  $K_m$  is the Michaelis–Menten constant for the variable substrate, and  $K_i$  is the substrate inhibition constant. The results are listed in Table 1.

#### 2.5. SHM reaction with glycine and 5,10-CH<sub>2</sub>-THF as substrates

The glycine + 5,10-CH<sub>2</sub>-THF → L-serine + THF (Gly → Ser) SHM activity was measured with 2 μM enzyme with glycine and CH<sub>2</sub>-THF as substrates. A directed coupled spectrophotometric assay was used in which the NAD<sup>+</sup>-dependent L-serine dehydrogenase from *Pseudomonas aeruginosa* oxidizes L-serine (produced by SHM) into 2-aminomethylmalonate semialdehyde (Tramonti et al., 2018). Assays were carried out at 30 °C in 50 mM TRIS-HCl pH 8.8. Saturation curves, obtained by varying either glycine or 5,10-CH<sub>2</sub>-THF concentration while keeping the other substrate fixed at a saturating concentration, were fitted to the Michaelis–Menten equation. The results are listed in Table 2.

#### 2.6. Determination of *A. thaliana* SHM structures

Purified proteins were concentrated (to ~15 mg/mL concentration) and subjected to crystallization in a sitting-drop vapor diffusion setup. AtSHM2 was crystallized in 90% of Index F8 condition (Hampton Research) containing 0.2 M ammonium sulfate, 0.1 M HEPES-NaOH pH 7.5, and 25% polyethylene glycol (PEG) 3350. The drop contained 3 μL of the protein solution and 2 μL of the reservoir solution. Cryoprotection was obtained by washing the crystal in the crystallization solution supplemented with 20% ethylene glycol. AtSHM4 crystallized in Index D9 condition (0.1 M Tris-HCl, pH 8.5, 25% PEG3350); the crystals were cryoprotected as for AtSHM2. The structure of AtSHM6 results from a crystal grown in 0.18 M Ammonium nitrate, 0.09 M Sodium cacodylate 5.3, 20% v/v PEG Smear Low, 10% ethylene glycol (based on the D1 condition of the BCS screen, Molecular Dimensions). Cryoprotection was

**Table 1**  
Steady-state kinetic parameters of AtSHM isoforms in the Ser → Gly reaction.

Isoform	$K_M$				
	pH	L-Ser (mM)	THF (μM)	$k_{\text{cat}}$ (s <sup>-1</sup> )	$K_i$ THF (μM)
AtSHM1	7.0	3.7 ± 0.3	84 ± 12	9.2 ± 2.1	198 ± 8
	8.0	2.1 ± 0.2	232 ± 76	20.0 ± 4.0	199 ± 29
AtSHM2 <sup>a</sup>	7.0	8.0 ± 1.4	154 ± 14	8.1 ± 0.7	191 ± 9
	8.0	2.9 ± 0.3	143 ± 12	13.0 ± 0.7	186 ± 12
AtSHM3	7.0	2.3 ± 0.4	148 ± 49	13.3 ± 4.0	62 ± 22
	8.0	3.6 ± 0.7	321 ± 109	13.3 ± 4.0	141 ± 46
AtSHM4 <sup>a</sup>	7.0	0.5 ± 0.05	14 ± 2	16.2 ± 1.1	57 ± 6
	8.0	0.30 ± 0.02	24 ± 4	17.4 ± 1.7	141 ± 23

<sup>a</sup> Values from (Ruszkowski et al., 2019).

**Table 2**

Steady-state kinetic parameters of AtSHM isoforms in the Gly → Ser reaction.

Isoform	$K_M$			
	pH	Gly (mM)	CH <sub>2</sub> -THF (μM)	$k_{\text{cat}}$ (min <sup>-1</sup> )
AtSHM1	8.8	0.69 ± 0.15	155 ± 22	10.4 ± 0.4
AtSHM2	8.8	0.20 ± 0.02	73 ± 9	7.9 ± 0.2
AtSHM3	8.8	0.52 ± 0.09	96 ± 14	7.2 ± 0.3
AtSHM4	8.8	0.19 ± 0.03	77 ± 13	4.8 ± 0.2

obtained by increasing the ethylene glycol concentration to 20% in the drop with the crystals. Crystals of AtSHM7 were obtained using the BCS screen, G8 condition (75 mM magnesium chloride, 75 mM sodium citrate tribasic, 0.1 M Bis-Tris pH 6.0, 18% v/v PEG Smear Broad); the same condition supplemented with 25% ethylene glycol was used for cryoprotection.

Diffraction data were processed with XDS (Kabsch, 2010). Data collection details and processing statistics are listed in Table 3. The AtSHM6 and AtSHM7 datasets were additionally submitted to anisotropic analysis using the STARANISO server (<http://staraniso.globalphasing.org/cgi-bin/staraniso.cgi>, Cambridge, United Kingdom, Global Phasing Ltd.). Anisotropically truncated data were used for structure solution and refinement. The structures were solved by molecular replacement in PHASER (McCoy et al., 2007), using a single subunit of

**Table 3**

Diffraction data collection and refinement statistics.

	AtSHM2	AtSHM4	AtSHM6	AtSHM7
Data collection				
Beamline	APS 22-ID	APS 22-ID	PETRA III P14	APS 22-ID
Wavelength (Å)	1.0000	1.0000	0.9763	1.0000
Space group	<i>P</i> 2 <sub>1</sub> 2 <sub>1</sub> 2 <sub>1</sub>	<i>P</i> 2 <sub>1</sub>	<i>P</i> 6 <sub>4</sub> 22	<i>C</i> 2
Unit cell parameters	115.2, 131.2, 151.4	59.0, 130.8, 121.7	129.7, 129.7, 302.3	199.8, 123.0, 290.5
<i>a</i> , <i>b</i> , <i>c</i> (Å)		β = 92.3°		β = 93.2°
β (°)				
Resolution (Å)	70.0–1.65	100.0–1.74	105.3–2.18 <sup>b</sup>	58.0–2.74 <sup>b</sup>
Unique reflections	274997 (43063)	181530 (29467)	49107 (2456)	121503 (6069)
Multiplicity	8.04 (6.39)	2.66 (2.58)	38.5 (34.4)	4.00 (4.36)
Completeness (%)	99.5 (97.0)	95.5 (96.0)	96.1 (80.6) <sup>c</sup>	93.5 (65.3) <sup>c</sup>
$R_{\text{meas}}$ <sup>a</sup> (%)	9.4 (113.9)	7.7 (59.2)	7.8 (221.3)	10.6 (62.7)
$\langle I/\sigma(I) \rangle$	17.19 (1.9)	8.60 (2.0)	29.8 (2.2)	10.9 (2.9)
Refinement				
$R_{\text{free}}$ reflections	1238	1090	981	1220
No. of atoms (non-H)				
protein	15069	14688	6720	41440
ligands	160	32	4	0
solvent	2116	1872	127	256
$R_{\text{work}}/R_{\text{free}}$ (%)	15.8/17.8	16.2/20.1	20.7/23.0	18.7/22.7
Average B-factor (Å <sup>2</sup> )	25	28	65	77
Rmsd from ideal geometry				
bond lengths (Å)	0.01	0.01	0.01	0.01
bond angles (°)	1.0	1.0	0.9	1.6
Ramachandran statistics (%)				
favoured	97	97	96	96
allowed	3	3	4	4
outliers	0	0	0	0
PDB ID	7pzz	7q00	7qpe	7qx8

Values in parentheses refer to the highest resolution shell.

<sup>a</sup>  $R_{\text{meas}}$  = redundancy independent R-factor.

<sup>b</sup> Best anisotropic diffraction limit cut-off.

<sup>c</sup> Provided values refer to ellipsoidal completeness. Spherical completeness is 62.0 (11.4) for AtSHM6 and 65.8 (11.5) for AtSHM7.

the MtSHMT3 structure (PDB ID: 6dc0, Ruskowski et al., 2018). The initial models were built in *Phenix.AutoBuild* (Terwilliger et al., 2008). Achesym was used to place the model inside the crystallographic unit cell (Kowiel et al., 2014). COOT (Emsley et al., 2010) was used for manual model corrections in the electron density maps between refinements in *Phenix.refine* (Afonine et al., 2012).

### 2.7. Size exclusion chromatography

Comparative size exclusion chromatography was performed using AKTA setup (GE Healthcare) and the Superdex200 16/60 column. The system was equilibrated in 25 mM HEPES-NaOH, pH 7.5, 100 mM KCl, 50 mM NaCl, 1 mM TCEP. Identical volumes (2.2 mL) of each protein were injected, and the chromatography was run using the same preset. Protein retention was monitored by recording absorbance at 280 nm.

### 2.8. Bioinformatic analyses

Tissue-specific expression data of *AtSHM* genes were retrieved from the Electronic Fluorescence Pictograph browser (eFP Arabidopsis) at [http://www.bar.utoronto.ca/\(Winter et al., 2007\)](http://www.bar.utoronto.ca/(Winter et al., 2007)). Collected experimental expression data came from the AtGenExpress Consortium, as well as from a tissue-specific collection, mirrored in the Bio-Array Resource (Toufighi et al., 2005). Genes co-expressed with *AtSHM* isoforms were screened using Genevestigator (Nebion), in the “Anatomy” and “Perturbation” modalities (Table 4, Supplementary Tables 2.1–2.7).

In the lack of experimental structures of *AtSHM1*, *AtSHM3*, and *AtSHM5*, we built their models based on the AlphaFold (Jumper et al., 2021) predictions retrieved from the AlphaFold database (referred to as SHM#-AF). As those are presented in a monomeric form, the functional tetramers were created by copying the subunit coordinates onto the tetramer, that is the closest homolog whose experimental structure was available. Specifically, *AtSHM1*-AF was truncated before Ser43 and superposed onto the experimental structure of *AtSHM2* (this work). *AtSHM3*-AF, truncated before Phe78, was superposed onto the crystal structure of *MtSHMT3* (PDB ID: 6dc0), which is also chloroplastic (Ruskowski et al., 2018). The full-length *AtSHM5*-AF model was superposed onto *AtSHM4* (this work).

The charge distribution on the protein surface was calculated in *PDB2PQR* and *APBS* (Baker et al., 2001; Dolinsky et al., 2004). The calculations were made at pH values characteristic of organelles where the isoforms localize (mitochondria, 8.1; cytosol, 7.3; nucleus, 7.2; (Shen et al., 2013); chloroplast, 8.0, corresponding to the illuminated stroma (Heldt et al., 1973; Hauser et al., 1995)).

## 3. Results and discussion

### 3.1. Gene expression in plant organs and tissues

To gain insight into the tissue-specific *AtSHM* expression profiles, we analyzed data openly available in eFP Arabidopsis at [http://www.bar.utoronto.ca/\(Winter et al., 2007\)](http://www.bar.utoronto.ca/(Winter et al., 2007)). This dataset contains gene expression data for different plant organs and at various growth stages. To our knowledge, the data regarding *AtSHM* isoforms have never been analyzed in literature. Between organs and within organs, *AtSHM* genes *At4g37930*, *At5g26780*, *At4g32520*, *At4g13930*, *At4g13890*, *At1g22020*, *At1g36370* (gene IDs for *AtSHM1*–7 genes, respectively) present diversified expression patterns (Fig. 1).

The *AtSHM1* gene was expressed at the highest levels in most analyzed tissues (Fig. 1). The exceptions were roots, flower petals, and top of the stem, where *AtSHM4* and *AtSHM5* were predominant or at the same level, as well as dry and imbibed seeds, where the expression of *AtSHM2* and *AtSHM3* was the highest. The second most abundant genes in most tissues were *AtSHM4* and *AtSHM5*. It is important to note that the most abundant *AtSHM* genes, *AtSHM1* and *AtSHM4*, are controlled by the circadian clock (Mcclung et al., 2000).

**Table 4**

Main functions of genes co-expressed with each *AtSHM* isoform.

Isoform	Main functions of the co-expressed genes
<i>AtSHM1</i>	<p><b>Photorespiration</b> (e.g., Glutamate–glyoxylate aminotransferase 1; Phosphoglycolate phosphatase 1A)</p> <p><b>Photosynthesis:</b> -regulation of the cyclic electron flow (Protein PROTON GRADIENT REGULATION 5) -light harvesting (eg. Photosystem I light harvesting complex gene 5) -photosynthetic electron chain (eg. Photosynthetic NDH subunit of subcomplex B 1; Ferredoxin–NADP reductase, leaf isozyme 2) -Calvin Cycle (eg. Sedoheptulose-1,7-bisphosphatase; Phosphoribulokinase)</p>
<i>AtSHM2</i>	<p><b>Mitochondrial respiration</b> (e.g., Gamma carbonic anhydrase-like 1; NADH dehydrogenase [ubiquinone] flavoprotein 2)</p> <p><b>Carbohydrate metabolism and glycolysis</b> (e.g., Pyrophosphate–fructose 6-phosphate 1-phosphotransferase subunit alpha 1)</p> <p><b>ATP binding, microtubule binding, microtubule motor activity</b> (e.g., Kinesin-2; ATP binding microtubule motor family protein)</p>
<i>AtSHM3</i>	<p><b>ATP binding, hydrolase activity, nucleic acid binding, RNA helicase activity</b> (e.g., DEAD-box ATP-dependent RNA helicase 10; DEAD-box ATP-dependent RNA helicase 22; DEAD-box ATP-dependent RNA helicase 51)</p> <p><b>Ribosome structural protein</b> (Ribosomal protein L7Ae/L30e/S12e/Gadd45 family protein; Ribosomal protein S5)</p> <p><b>Methylation</b> (e.g., Protein arginine N-methyltransferase 1.5; Protein arginine N-methyltransferase 1.1; S-adenosyl-L-methionine-dependent methyltransferases superfamily protein)</p> <p><b>DNA binding</b> (e.g., DNA topoisomerase, type IA, core; Single-stranded DNA-binding protein WHY2)</p>
<i>AtSHM4</i>	<p><b>S-adenosyl-L-methionine biosynthesis</b> (e.g., S-adenosylmethionine synthase 3; S-adenosylmethionine synthase 4)</p> <p><b>Recycling of S-adenosylmethionine-dependent methylation</b> (e.g., Adenosine kinase 1; Adenosine kinase 2; Adenosylhomocysteinase 2).</p> <p><b>Methionine formation</b> (e.g., MS2:5-methyltetrahydropteroyltriglutamate–homocysteine methyltransferase 2)</p> <p><b>TCA cycle, carbohydrate metabolism and glycolysis:</b> Malate dehydrogenase 1; Pyrophosphate–fructose 6-phosphate 1-phosphotransferase subunit alpha 1; 2,3-bisphosphoglycerate-independent phosphoglycerate mutase 1</p>
<i>AtSHM5</i>	<p><b>Protein ubiquitination</b> (e.g., RING/U-box superfamily protein; ARM repeat superfamily protein; RING/FYVE/PHD zinc finger superfamily protein; Ubiquitin-associated/translation elongation factor EF1B protein; MATH domain-containing protein; Ubiquitin fusion degradation UFD1 family protein)</p> <p><b>Histone binding, regulation of DNA methylation, chromatin organization</b> (agenet domain-containing protein/bromo-adjacent homology (BAH) domain-containing protein)</p> <p><b>Transcription elongation factor activity</b> (e.g., Transcription elongation factor (TFIIS) family protein)</p>
<i>AtSHM6</i>	<p><b>Sulfate reduction for Cys biosynthesis</b> (e.g., 5'-adenylylsulfate reductase 1; 5'-adenylylsulfate reductase 2; 5'-adenylylsulfate reductase 3)</p> <p><b>Cellular response to sulfur starvation, regulation of glucosinolate biosynthetic process</b> (e.g., Protein SULFUR DEFICIENCY-INDUCED 1; Protein SULFUR DEFICIENCY-INDUCED 2; response to low sulfur 2).</p> <p><b>Protein ubiquitination</b> (U-box domain-containing protein 17)</p> <p><b>ATP binding, ATP hydrolysis</b> (AAA-type ATPase family protein)</p>
<i>AtSHM7</i>	

Contrary to *AtSHM1*, the other mitochondrial isoform, *AtSHM2*, is not expressed (or expressed at a very low level) in mesophyll cells where photosynthesis takes place (Fig. 1B). Engel et al. (2011) showed that the presequence of *AtSHM2* precludes targeting into mesophyll mitochondria in leaves. Exchange of the *AtSHM2* presequence with that of *AtSHM1* could fully replace *AtSHM1* activity in photorespiratory

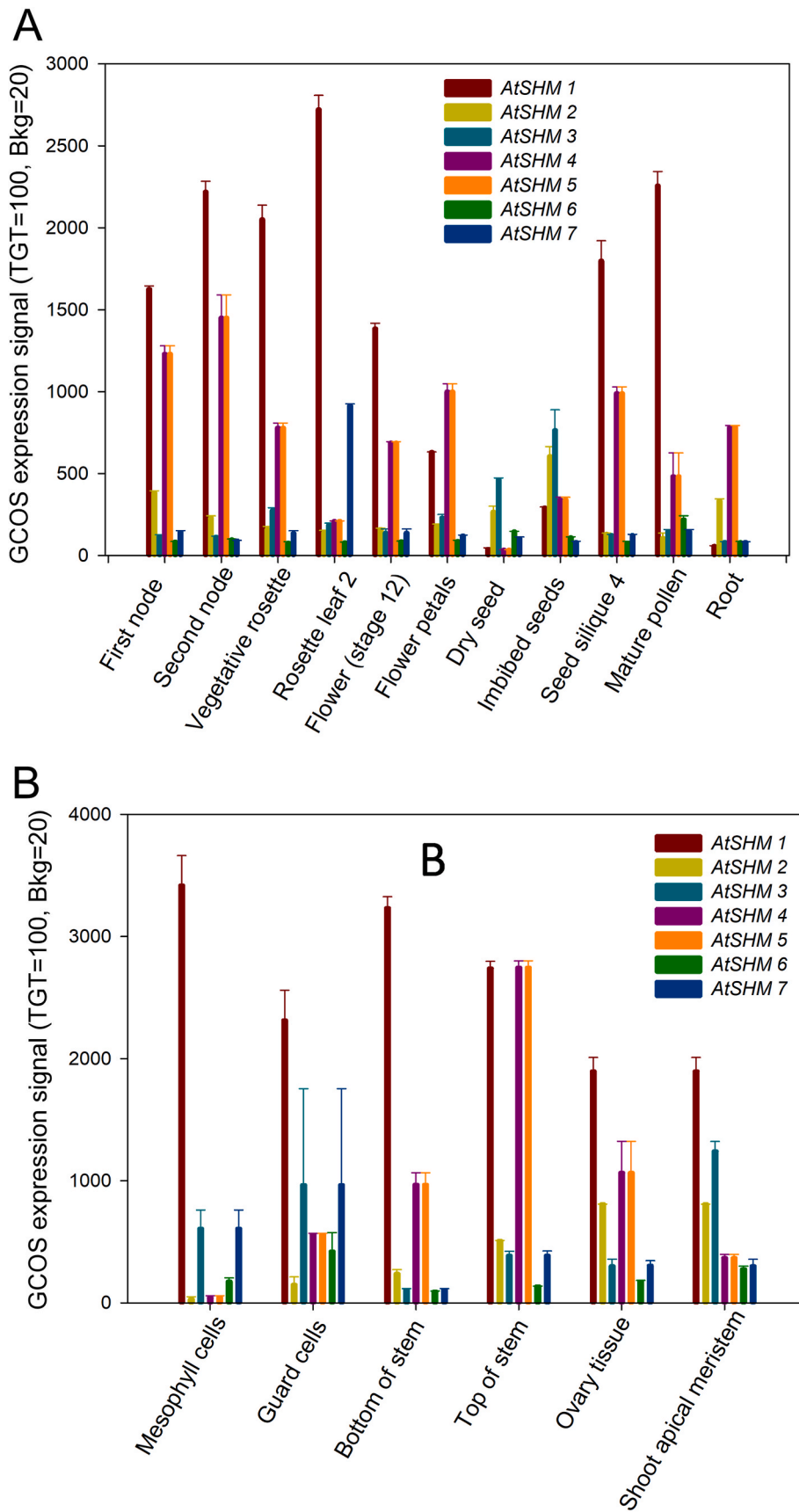


Fig. 1. Expression patterns of the *AtSHM* genes across several tissues collected from the Electronic Fluorescence Pictograph browser (eFP Arabidopsis) with Developmental Map (A) and Tissue Specific (B) data sources at <http://www.bar.utoronto.ca/>.

metabolism. The authors detected *AtSHM2* expression in the vasculature of leaves (in heterotrophic cells), where *AtSHM2* occurs together with *AtSHM1* but not in mesophyll cells. Because there is a high demand for one-carbon units in *Arabidopsis* vascular tissues, the authors suggested involvement of *AtSHM2* in the lignification processes. On the other hand, *AtSHM2* is normally imported into mitochondria of other tissues (Engel et al., 2011). eFP *Arabidopsis* shows that *AtSHM2* expression occurs mainly in the shoot apical meristem, imbibed seeds, top of the stem, ovary tissue, roots, and first node (Fig. 1).

The plastid-targeted *AtSHM3* is mainly expressed in the shoot apical meristem, seeds (imbibed and dry), as well as in guard and mesophyll cells. Curiously, although this isoform is apparently localized in chloroplasts (Zhang et al., 2010), its expression in leaves is lower than that of *AtSHM1* (Fig. 1). In plastids, SHM could participate in the synthesis of a light-harvesting cofactor in a plastid-localized cryptochrome (Zhang et al., 2010), in addition to generating one-carbon units for the biosynthesis of purines, thymidylate and *N*-formylmethionine.

The two cytosolic *AtSHM4* and *AtSHM5* were in general highly expressed except for rosette leaf 2, dry seed, shoot apical meristem, and mesophyll cells (Fig. 1). However, we acknowledge that *AtSHM4* and *AtSHM5* display the same gene expression pattern, which is unusual and may be due to their close location on chromosome 4 (Zhu et al., 2003) or indicate an issue with primers specificity. Nonetheless, Boavida et al. (2009) correlated an *A. thaliana* *Ds* insertional mutant line in gene *AtSHM5* with a defect in male gametophyte development. Pagnussat et al. (2005) identified defects in female gametophyte development in two insertional mutant lines in the gene *At4g13890* (*AtSHM5*). It is also interesting to note that *A. thaliana* plants overexpressing *AtSHM4* have longer roots than wild-type plants (Patent EP 3222729 A3).

The nuclear isoforms, *AtSHM6* and *AtSHM7* were generally the least expressed genes. However, in leaves (mesophyll, guard cells, and rosette leaf 2), the expression of *AtSHM7* was actually second to *AtSHM1* (Fig. 1). *AtSHM7* has been linked to the regulation of DNA methylation, sulfate ion homeostasis, and SAM metabolism, as the *AtSHM7* loss of function results in decreased SAM, DNA methylation levels, and S-deficiency response (Huang et al., 2016). Zhang et al. (2017), using a computational method, i.e., random walk with restart algorithm applied on a protein-protein interaction network, identified *AtSHM6*, *AtSHM7*, and *AtSHM5* (cytosolic) as genes related to fruit development and maturation. However, the molecular mechanisms behind the functions of *AtSHM5*, *AtSHM6*, and *AtSHM7* proteins remain unknown.

To ascertain the involvement of *AtSHMs* in cellular processes, we used Genevestigator (Nebion) to identify genes that are co-expressed with *AtSHMs*. The summary is given in Table 4, whereas Supplementary Tables 2.1–2.7 include details for each *AtSHM* isoform in the “Anatomy” and “Perturbation” modalities. Genes expressed together with *AtSHM1* further support its role in photorespiration, while *AtSHM2* appears linked to mitochondrial respiration. *AtSHM3* is co-expressed with genes of most diverse functions, which is consistent with the presence of only one *AtSHM* isoform in the chloroplast. With *AtSHM4–5*, the aforementioned ambiguity issue is also apparent but they are linked with methionine and SAM biosynthesis and recycling. Regarding the nuclear isoforms, *AtSHM6* is co-expressed with genes involved e.g., in ubiquitination, histone binding, DNA methylation, suggesting important regulatory roles for this isoform. Finally, *AtSHM7* accompanies genes participating in sulfur metabolism, which is consistent with the work of Huang et al. (2016) who have linked *AtSHM7* with maintaining sulfur homeostasis.

### 3.2. Catalytic properties of *AtSHM* isoforms

We purified and characterized all *AtSHMs* under the same conditions to compare their catalytic properties *in vitro* (Tables 1 and 2). The purified samples of *AtSHM5* and *AtSHM6* were light yellow, and their spectra showed a small peak at 420 nm (characteristic of the internal aldimine Schiff base formation between PLP and an amino group of

lysine residue of the enzyme) compared to the other *AtSHM* isoforms that presented a higher 420 nm peak (data not shown). Since the 420 nm band corresponds to PLP covalently bound to the enzyme as a Schiff base (Ruszkowski et al., 2019), this observation indicates that the purified *AtSHM5* and *AtSHM6* are mostly in the apo-form. *AtSHM7* showed a canonical spectrum with the characteristic absorbance band at 420 nm just after purification (Supplementary Fig. S1). The spectrum changed after 1 day as the 420 nm absorbing band was converted into a 330 nm absorbing band.

The Ser → Gly reaction was measured at 30 °C at two different pH values, pH 7.0 and pH 8.0. This pH range corresponds to the milieu in cellular compartments where SHMs are localized; cytosol, pH 7.3; mitochondria, pH 8.1; nucleus, pH 7.2 (Shen et al., 2013); chloroplast (illuminated stroma), 8.0 (Heldt et al., 1973; Hauser et al., 1995). Analysis of the saturation curves (Supplementary Figs. S2 and S3) yielded the steady-state kinetic parameters listed in Table 1. Our results confirm that *AtSHM5*, *AtSHM6*, and *AtSHM7* are inactive as SHM, as previously reported (Wei et al., 2013; Huang et al., 2016). Noteworthy, assays with *AtSHM7* were performed just after the purification. Moreover, incubation of the purified proteins with PLP (final concentration 100 μM), followed by subsequent dialysis, failed to rescue SHM activity. To check whether inactivity was due to weak PLP binding, we also performed the assays including exogenous PLP (final concentration 100 μM) in the mixture; however, SHM activity was non-detectable even in this case. Thus, the question remains why *AtSHM5–7* are inactive, suggesting a different biological function, as they may not be *bona fide* SHM enzymes. Perhaps they could bind RNAs, which would give them regulatory functions similar to the human cytosolic (HsSHMT1) isoform (Guiducci et al., 2019) or form multi-protein complexes. In this regard, it has been reported that yeast SHM2 takes part in SESAME, a protein complex that links serine metabolism with histone modification (Li et al., 2015). Since *AtSHM6–7* exist in the nucleus, other regulatory mechanisms, such as DNA binding, cannot be excluded.

The results show that the activity of *AtSHM(1–4)* isoforms is pH-sensitive. With the exception of the plastidic *AtSHM3* isoform,  $k_{cat}$  values, extrapolated at saturating THF concentration, increase with pH (Table 1). The  $k_{cat}$  value of *AtSHM3* is unaffected by the change in stromal pH stimulated by light (Heldt et al., 1973; Hauser et al., 1995). *AtSHM1* and *AtSHM4* have the highest turnover rates at pH 8.0. *AtSHM4* is also significantly more specific towards both substrates, making it the most catalytically efficient isoform due to low  $K_M$  and high  $k_{cat}$  values. Considering only the mitochondrial isoforms, the  $k_{cat}$  of *AtSHM1* is higher than that of *AtSHM2* at both pH values. The  $K_M$  for THF is unaffected by pH only for *AtSHM2*, whereas for all other isoforms it increases with pH. On the contrary,  $K_M$  for L-Ser decreases with increasing pH for all *AtSHMs* except for *AtSHM3*.

We also determined the THF substrate inhibition constants ( $K_i$ , Table 1). In other species, THF inhibits SHMs via the formation of an enzyme-glycine-THF dead-end complex, which may enable SHM activity regulation (Tramonti et al., 2018). The  $K_i$ (THF) for both mitochondrial SHMs is similar and insensitive to pH fluctuation (at 7.0 and 8.0). However, for *AtSHM3* and *AtSHM4*  $K_i$ (THF) increases ~2.5 fold with increasing pH. Altogether, *AtSHM3* and *AtSHM4* are much more sensitive to THF inhibition at pH 7.0 than *AtSHM1* and *AtSHM2*, whereas at pH 8.0 all isoforms exhibit similar  $K_i$ (THF).

Overall, *AtSHM4* has the highest efficiency in the Ser → Gly conversion and also the lowest  $K_M$  for both substrates. *AtSHM4* is also the most susceptible to THF inhibition, indicating a tight regulation of its activity. Substrate inhibition often has important biological functions (Reed et al., 2010). In folate metabolism, substrate inhibition is most likely linked to folate storing. This seems to be the case, especially for *AtSHM4*, considering that folates in leaf cells are mostly localized in the cytosol (Gambonnet et al., 2001). In the study on the chloroplastic SHM from *M. truncatula* (*MtSHMT3*), we suggested a mechanism to control substrate inhibition in SHM (Ruszkowski et al., 2018). Accordingly, a pair of tyrosines in the vicinity of the active site forms a molecular gate,

which accepts THF at the reaction stages when THF is required, *i.e.*, the external aldimine states (Ruszkowski et al., 2018). Minute changes in the SHM regions surrounding the tyrosine pair may allow fine-tuning of the THF inhibition. Importantly, the tyrosine pair is conserved not only in plant SHM but also in other kingdoms.

The Gly → Ser reaction was measured by a spectrophotometric coupled assay in which the L-serine product is oxidized to 2-aminomethylmalonate semialdehyde by the NAD<sup>+</sup>-dependent L-serine dehydrogenase from *P. aeruginosa* (Tramonti et al., 2018). Assays were carried out at pH 8.8 to ensure optimal turnover of L-serine dehydrogenase (Supplementary Fig. S4). Steady-state kinetic parameters of AtSHMs with glycine and CH<sub>2</sub>-THF are shown in Table 2. AtSHM5-7 isoforms show no activity in the Gly → Ser reaction, as observed in the Ser → Gly reaction. This further highlights the question whether AtSHM5-7 should still be classed as SHMs? AtSHM1 is the isoform with the highest  $k_{cat}$  value. It also presents the highest  $K_M$  for both substrates, Gly and 5, 10-CH<sub>2</sub>-THF. AtSHM4 is the slowest in the Gly → Ser reaction but it shows low  $K_M$  for both substrates, similar to AtSHM2. Regarding the role of the Gly → Ser reaction in photorespiration, it is known that Gly produced in peroxisomes during photorespiration mobilizes within leaves and accumulates in the cytosol, chloroplast and mitochondria (Keys, 1999; Noctor et al., 1999). Gly/Ser ratio in *Arabidopsis* leaves under photorespiratory conditions is around 0.5 but it largely decreases in extended darkness, when photorespiration is limited (Sipari et al., 2020), and increases under high photorespiratory conditions (e.g. low CO<sub>2</sub>, (Dellero et al., 2021)). Thus, assuming that Gly/Ser ratio is similar in the whole leaf and in the mitochondria, Gly → Ser reaction may be favorable only under photorespiratory conditions.

### 3.3. Structures of *A. thaliana* SHMs

Within this work, we have determined four new crystal structures of AtSHM2 (Nt41), AtSHM4, AtSHM6 (Nt127), and AtSHM7 (Nt123); “Nt” denotes the N-terminal residue after truncation of the signal peptide. Statistics of the data collection and structure refinement are listed in

Table 3. The maps quality for AtSHM2 (1.65 Å resolution) is excellent; the structure contains a tetramer in the asymmetric unit (ASU). The final model contains the protein residues starting from Arg44 (or before, chain-dependent) until the C-terminus (Glu517). The only missing fragment in the AtSHM2 structure is Ser422-Ala423 of chain C. The structure of AtSHM4, determined at 1.74 Å resolution, contains one tetramer in the ASU. The C-terminal Asp471 is missing only in chain A, whereas the rest of the protein chain was traced in the electron density maps unambiguously. Both AtSHM2 and AtSHM4 contain the PLP prosthetic group bound in the form of internal aldimine to Lys286 and Lys244, respectively. The ASU of the AtSHM6 structure (2.18 Å resolution) contains half of the tetramer in the ASU; the full tetramer is restored by symmetry operations. There are three poorly defined regions in the electron density maps which have not been modeled between Pro260-Lys276, Pro392-Ile406, and Ala557-Lys576. PLP, expected at Lys374, was not placed due to lack of convincing electron density. The quality of the AtSHM7 structure, determined at 2.74 Å resolution, is worse but sufficient to build the model with satisfactory geometric parameters. The ASU contains three tetramers, with all chains lacking PLP, expected at Lys370. Discontinuous electron density disabled modeling of fragments containing residues 257–270, 388–400, and 510–511 (approximate ranges, chain-dependent).

We have analyzed the oligomeric state of all seven AtSHM isoforms using size-exclusion chromatography (Supplementary Fig. S5). The elution profiles were compared to that of HsSHMT1, known to form homotetramers (Renwick et al., 1998). Based on this experiment, all AtSHM isoforms are tetramers in solution. Structural analysis shows that the tetramers have D<sub>2</sub> symmetry and are formed by two tight dimers (Fig. 2). It is of note that most mammalian SHM homologs also form tetramers, as reported for the rabbit (Scarsdale et al., 1999) and mouse (Szebenyi et al., 2000) proteins. The same applied to the chloroplastic MtSHMT3 reported previously (Ruszkowski et al., 2018). On the other hand, in the human mitochondrial SHMT2, the dimer-to-tetramer transition is triggered by PLP-binding (Giardina et al., 2015). However, SHMTs from lower eukaryotes and from prokaryotes usually form

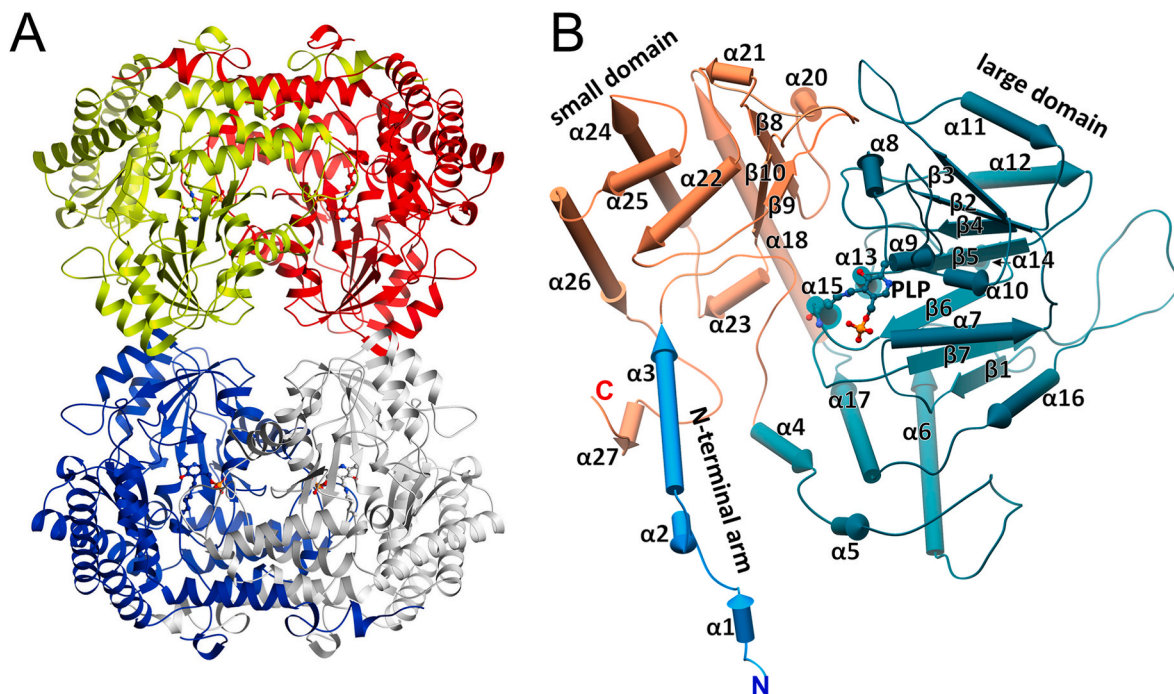


Fig. 2. Overall structure of AtSHM. The crystal structure of AtSHM4 (PDB ID: 7q00) is presented. Panel A shows AtSHM4 tetramer, colored per subunit. Secondary structure elements depicted as pipes and planks on a single AtSHM4 subunit are shown in panel B. The N-terminal arm, the large domain and the small domain are colored blue, green, and orange, respectively. PLP (as internal aldimine, ball-and-stick model) is shown to indicate location of the active site. All helices are labeled as  $\alpha$  (regardless of the type) for clarity.

dimers (Scarsdale et al., 2000; Angelaccio et al., 2014; Chitnumsub et al., 2014a, 2014b; Nogués et al., 2020). Each tight dimer of AtSHM resembles an SHM dimer from lower eukaryotes or prokaryotes (not shown). Formation of the dimer is actually obligate to form a complete active site, a feature that is common for all type I PLP-dependent enzymes (Liang et al., 2019).

To introduce the general subunit architecture, we use the cytosolic AtSHM4 isoform. All helices are labeled as  $\alpha$  (regardless of the type) for clarity. The subunit is made of the N-terminal arm, the large domain and the small domain (Fig. 2B), named according to the standards established for SHMs (Scarsdale et al., 2000). The N-terminal arm contains helices  $\alpha$ 1-3, and protrudes towards the other subunit of the tight (obligate) dimer. The large domain is folded into an  $\alpha\beta$  sandwich containing the seven-stranded mixed  $\beta$ -sheet ( $\beta$ 1 $\uparrow$ - $\beta$ 7 $\downarrow$ - $\beta$ 6 $\uparrow$ - $\beta$ 5 $\downarrow$ - $\beta$ 4 $\uparrow$ - $\beta$ 2 $\downarrow$ - $\beta$ 3 $\uparrow$ ). The  $\beta$ -sheet is shielded by helices  $\alpha$ 8,  $\alpha$ 9,  $\alpha$ 10,  $\alpha$ 7,  $\alpha$ 16 from one side and by  $\alpha$ 11,  $\alpha$ 12,  $\alpha$ 13,  $\alpha$ 14,  $\alpha$ 6 from the other. The PLP prosthetic group is bound within the large domain. Finally, the small domain is an  $\alpha\beta$  sandwich with an antiparallel  $\beta$ -sheet ( $\beta$ 8- $\beta$ 9- $\beta$ 10) shielded from solvent by helices  $\beta$ 18-26.

### 3.4. Structural differences between *A. thaliana* SHM isoforms

Sequence alignment of all isoforms (without the signal peptide and the variable extension of the N-terminal arm) shows that AtSHMs share only ~32% of identical residues and present ~64% sequence similarity; pairwise comparison is presented in Table 5. For structural analysis of the seven SHM isoforms in *A. thaliana*, all models (best-matching chains) were superposed onto the structure of AtSHM4. The resulting RMSD values are within 0.5–0.8 Å range for the pruned C $\alpha$  atom pairs within 2 Å distances and 1.0–2.1 Å for all C $\alpha$  pairs. This comparison revealed that while most of the protein fold is conserved, there are regions of significant variability (Fig. 3A and B). From the N-to-C termini, the first differences appear within the  $\alpha$ 1 helix, which is the longest in AtSHM6-7 and missing entirely in AtSHM3. The initial part of the N-terminal arm has been previously linked to stabilization of the tetrameric structure of sheep liver cytosolic SHM (Jagath et al., 1997); however, the sequence identity between sheep and plants in this region is very low.

The next variable element is the loop- $\alpha$ 9-loop fragment (Gly132-Ser148 in AtSHM4). It is particularly important as it includes the histidine residue (His134 in AtSHM4) that is conserved in all isoforms and  $\pi$ -stacks PLP when present (not shown). Surprisingly, the fragment is missing in the electron density maps in our AtSHM6 and AtSHM7 structures, which lack PLP but have water molecules bound as placeholders for a part of the loop- $\alpha$ 9-loop fragment. Notably, the fragment is present in the proteins, while its lack in the electron density can be attributed to multiple conformations causing disorder and “blurring” of the maps. Nonetheless, the reason for disturbed PLP binding by AtSHM6-7 remains an open question and is particularly perplexing given the high sequence conservation of the loop- $\alpha$ 9-loop region. A disorder-to-order transition caused by PLP binding has been observed in MtSHMT3, but in this case, it involved the C-end of the  $\alpha$ 6 helix equivalent (this work numbering) and the following loop that interacted with PLP of the dimer partner (Ruszkowski et al., 2018). Residues that precede the PLP-stacking histidine are more conserved than those which follow (not shown). Interestingly, the latter fragment interacts with the glutamyl

moiety of antifolates (Fig. 3C, (Ruszkowski et al., 2019)). In the mitochondrial isoenzymes (AtSHM1 and AtSHM2), this fragment is built of Y-Q-T-D-T, whereas the chloroplastic AtSHM3 has F-M-T-A-K sequence. A significantly different sequence occurs in cytosolic and nuclear AtSHMs, where it is one residue longer and has Y-Y/C-T/S-S/P-G-G pattern. The double glycine motif adds flexibility to the region, which could be compensated in nuclear isoenzymes by the preceding proline.

Another structural difference is apparent in the  $\beta$ 7- $\alpha$ 16 loop (Fig. 3). The loop is shorter in AtSHM3, spanning only eight residues (Lys328-Asp335). The corresponding fragment is 16 and 17 residues long in the mitochondrial (AtSHM1, AtSHM2) and cytosolic (AtSHM4, AtSHM5) isoforms, respectively. In both AtSHM6 and AtSHM7, the  $\beta$ 7- $\alpha$ 16 loop is extremely extended and spans 22 residues (Fig. 3A).

The  $\beta$ 9- $\beta$ 10 loop does not differ in length (12 residues in all isoforms) but shows variable conformation (Fig. 3A). The key conformation determinant appears to be the proline that occurs in AtSHM1-3 (e.g., Pro418 in AtSHM2) or phenylalanine in the remaining isoforms (e.g., Phe377 in AtSHM4 and Phe507 in AtSHM7).

The last variable fragment, labeled as loop- $\alpha$ 25-loop, spans residues Gly427-Asn440 in AtSHM4 (Fig. 3). The presence of the helix corresponding to  $\alpha$ 25 is universal in all isoforms. Still, its position differs by as much as 4.9 Å in two experimentally determined structures of AtSHM4 and AtSHM7 (C $\alpha$  atoms of conserved Phe433 and Phe564, respectively).

It is now exciting to note that when the SHM tetramer is considered, most variable fragments surround the active site of either the same subunit or another one (Fig. 3B and C). As stated above, the loop- $\alpha$ 9-loop fragment directly participates in the active site formation. Previously, based on modeling and sequence comparison, the highest catalytic efficiency of AtSHM4 was attributed to flexibility in region Pro130-Ile152, which includes the loop- $\alpha$ 9-loop fragment (Wei et al., 2013). However, the  $\beta$ 9- $\beta$ 10 loop and the loop- $\alpha$ 25-loop fragment shape the entrance to the active-site cavity (Fig. 3C). Also, the  $\beta$ 7- $\alpha$ 16 loop of the neighboring subunit (not within the swapped dimer) protrudes towards the active site entrance. This loop, together with its equivalent from the diagonal subunit in the tetramer, forms a lid-like structure (Fig. 3B and C). Therefore, the  $\beta$ 7- $\alpha$ 16 loop very likely interacts with the polyglutamylated tail of THF, thus controlling the preference of SHM isoforms towards folates with certain Glu<sub>n</sub> ranges. The striking difference in length of the  $\beta$ 7- $\alpha$ 16 loop (from 8 residues in AtSHM3 to 22 in AtSHM6-7) and high sequence variability may enable Glu<sub>n</sub> length selectivity in subcellular compartments. In summary, all variable fragments must be taken into account as they all have the potential to shape the functional landscape of SHM isozymes in *A. thaliana*.

We have also analyzed all residues within a 4 Å radius from PLP to answer why AtSHM5, AtSHM6, and AtSHM7 do not bind PLP or are inactive. First, AtSHM6 and AtSHM7 contain the Cys-Thr dipeptide (residues 236–237 and 232–233, respectively) instead of Gly-Ser, universally present in AtSHM1-5 nearby the phosphate of PLP. Neither of the cysteines corresponds to the Cys125-Cys364 pair involved in redox regulation of *Plasmodium falciparum* SHMT activity (Chitnumsub et al., 2014a). Based on the superposition of PLP (from AtSHM4) onto the AtSHM6-7 structures, the distance between the S atom and the ring centroid would be < 4 Å. While S-aromatic interactions are common in proteins, the distance is usually >5 Å (Reid et al., 1985); however, a small rearrangement should accommodate PLP. Furthermore, AtSHM6

**Table 5**

Sequence identity matrix of AtSHM isoforms (excluding the signal peptides and most structurally variable extension of N-terminal arm).

	AtSHM1	AtSHM2	AtSHM3	AtSHM4	AtSHM5	AtSHM6	AtSHM7
AtSHM1		88	62	57	56	52	52
AtSHM2	88		61	56	55	50	50
AtSHM3	62	61		61	57	53	53
AtSHM4	57	56	61		81	62	63
AtSHM5	56	55	57	81		60	60
AtSHM6	52	50	53	62	60		80
AtSHM7	52	50	53	63	60	80	

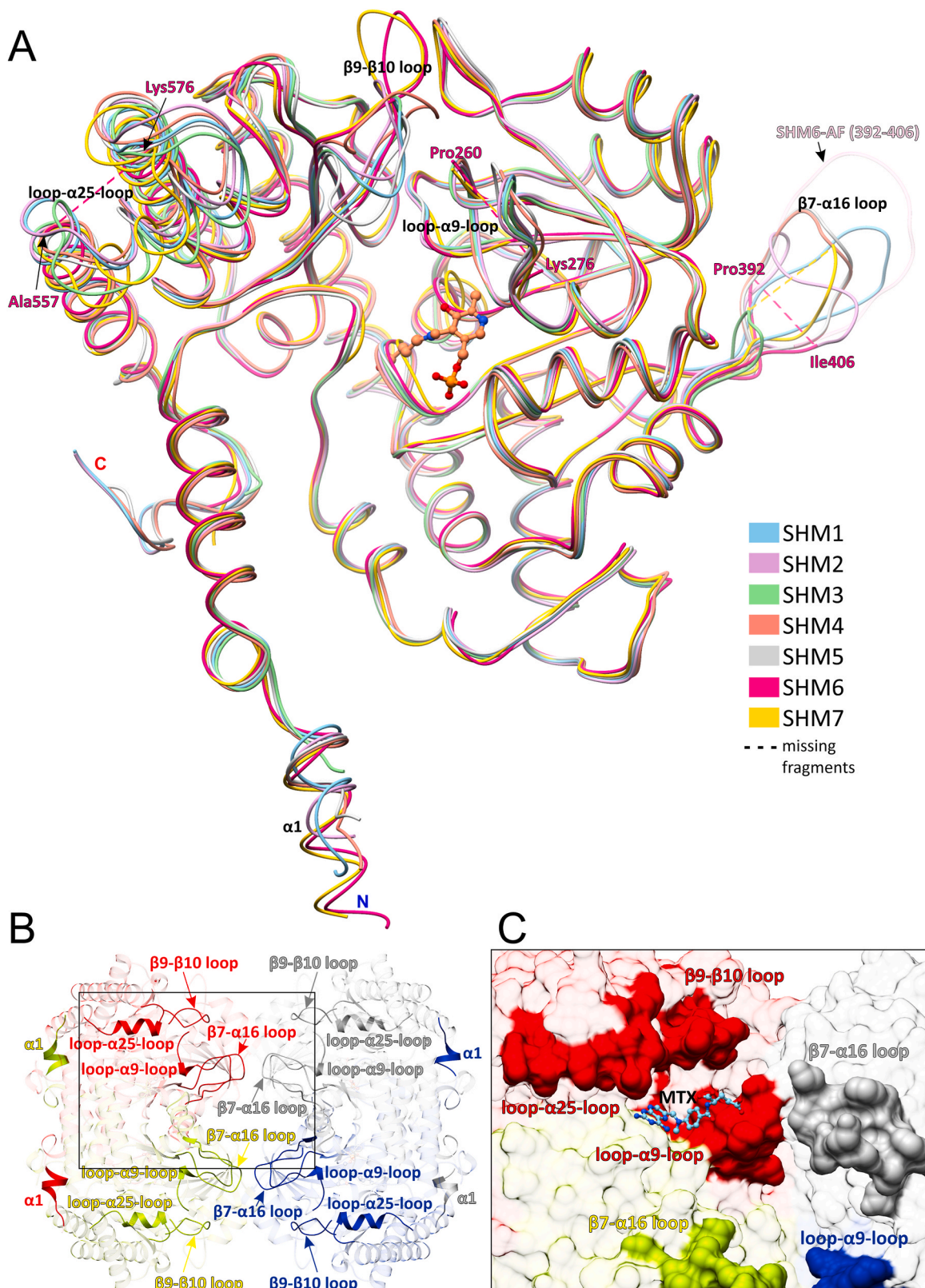


**Fig. 3.** Comparison of subunit structures of all *A. thaliana* SHM isoforms, color-coded as in the legend. Crystal structures are shown for SHM2, SHM4, SHM6, and SHM7 (this work), while AlphaFold (AF) DB predictions were used for the remaining three isoforms. The missing fragment 393–405 in the SHM6 crystal structure is shown using SHM6-AF model (semitransparent) to illustrate length of the  $\beta$ 7- $\alpha$ 16 loop in the nuclear SHM isoforms. Panel B shows location of the variable regions in the SHM tetramer (based on AtSHM4). The entrance to the active site cavity with a superposed methotrexate (MTX) from the complex with AtSHM4 (PDB ID: 6smr (Ruszkowski et al., 2019)) is shown in panel C to mark the approximate THF binding site.

contains Gln348, where all other isoforms, including AtSHM7, have a histidine residue. As for AtSHM5, which is strikingly similar to active AtSHM4, Thr190 in AtSHM5 lies where the other isoforms have a serine (Ser190 in AtSHM4); however, a Ser-Thr substitution is unlikely to impact the activity on its own. An opposite substitution occurs at Ser241 of AtSHM5, where other isoforms possess a threonine (e.g., Thr241 in AtSHM4). Ser289 in AtSHM5 substitutes a universal glycine residue (Gly289 in AtSHM4). In conclusion, it appears that the impaired PLP binding is due to a cumulative effect of multiple substitutions in the neighborhood of the (expected) PLP site, as none of the aforementioned mutations alone could provide a clear answer as to why AtSHM5-7 are inactive. Furthermore, the rationale appears different for AtSHM5 and for AtSHM6-7.

We also looked for post-translational modification (PTM) that could activate those isoforms. PTM data were retrieved from the Plant PTM Viewer (<https://www.psb.ugent.be/webtools/ptm-viewer>) (Willems et al., 2019) and the FAT-PTM database (<https://bioinformatics.cse.unr.edu/fat-ptm/>) (Cruz et al., 2019); the summary is given in Supplementary Table 3. However, acetylation at Lys435 in AtSHM5 occurs ~40 Å away from the active site and far from dimerization/tetramerization interfaces. Moreover, all PTMs regarding AtSHM6-7 occur within the putative signal peptide. In this context, it is key to recall that fragments revealing high sequence and structure variability appear either near the tunnel leading to the active site of a subunit (the  $\beta$ 9- $\beta$ 10 loop, loop- $\alpha$ 25-loop) or of a subunit at a tetramer diagonal (the  $\beta$ 7- $\alpha$ 16 loop). This suggests that the answer to the lack of SHM activity of isoforms AtSHM5-7 most likely lies in these fragments.

### 3.5. Charge distribution analysis

To shed more light on the peculiar features of *A. thaliana* SHM isoforms, we analyzed the electrostatic potential distribution on the protein

surface. The calculations were made at pH values characteristic of organelles where the isoforms localize (mitochondria, 8.1; cytosol; 7.3; nucleus, 7.2; (Shen et al., 2013); chloroplast, 8.0 (Heldt et al., 1973; Hauser et al., 1995). A side-by-side comparison (Fig. 4) shows that AtSHM5 stands out with the overall highly negative charge. This is consistent with the lowest calculated pI of AtSHM5 (5.7) among all AtSHM isoforms. Although AtSHM4 and AtSHM5 share high sequence identity (82%), their pIs differ substantially (6.8 vs 5.7, respectively). Several N(or Q)-to-D(or E) or uncharged-to-acidic residue substitutions map on the surface (not shown) of the proteins thus explaining the difference. The abundance of negatively charged residues on the protein surface may repel even non-polyglutamylated THF. Furthermore, in the AlphaFold model of AtSHM5, the entrance to the active-site cavity is blocked by the  $\beta$ 9- $\beta$ 10 loop (Fig. 5), mainly by Phe382. Both factors provide a convincing explanation as to why AtSHM5 lacks SHM activity.

AtSHM2 and AtSHM6 present a more extended patch of positive charge around the active site than the other isoforms. When comparing pairs of AtSHMs from the same cellular compartment (AtSHM1 vs. AtSHM2, AtSHM4 vs. AtSHM5, AtSHM6 vs. AtSHM7), one isoform (AtSHM2, AtSHM4, AtSHM6) always presents such an extended patch of positive potential around the active site (Fig. 4). These isoforms are, in general, characterized by higher pI; only nuclear AtSHM6 and AtSHM7 have almost identical pI (see Fig. 4 caption). The reason for AtSHM redundancy in subcellular compartments may allow for more precise handling of differently polyglutamylated folates or to engage one of the isoforms under stress when cellular conditions are altered (Gout et al., 2001). Moreover, the mitochondrial AtSHM1 shows nearly 3-fold lower  $K_M$  at pH 7 than at pH 8 (Table 1). The higher sensitivity of AtSHM1 to pH variations can also be explained by the surface charge, which in AtSHM2 remains positive across the tested range.

Looking at the vicinity of the active site, the loop  $\beta$ 7- $\alpha$ 16 in the mitochondrial SHMs (AtSHM1 and AtSHM2) contains an N-K-Q-G-K

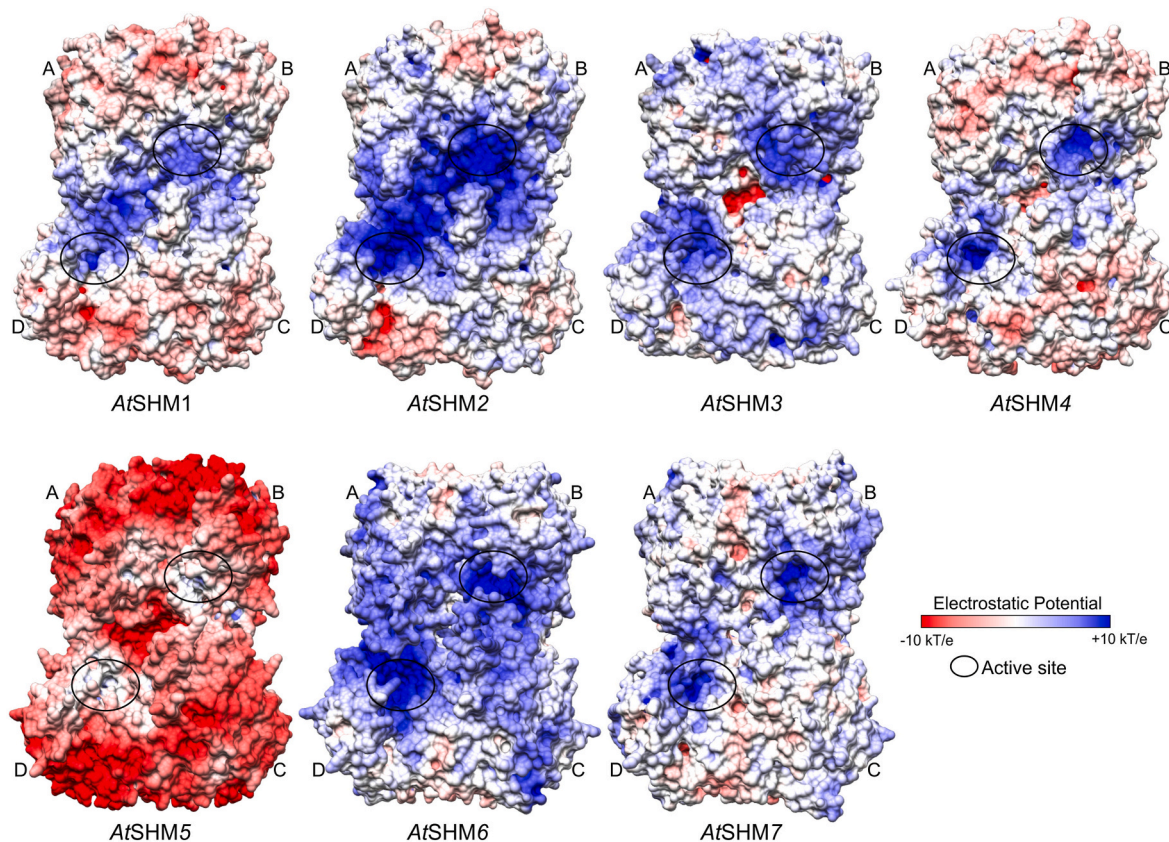


**Fig. 4.** Electrostatic potential on the surface of AtSHM isoenzymes. The approximate localization of the active site is marked with a circle. Theoretical pI for each isoenzyme is: AtSHM1 (6.9), AtSHM2 (8.2), AtSHM3 (8.4), AtSHM4 (6.8), AtSHM5 (5.7), AtSHM6 (8.3), AtSHM7 (8.3).

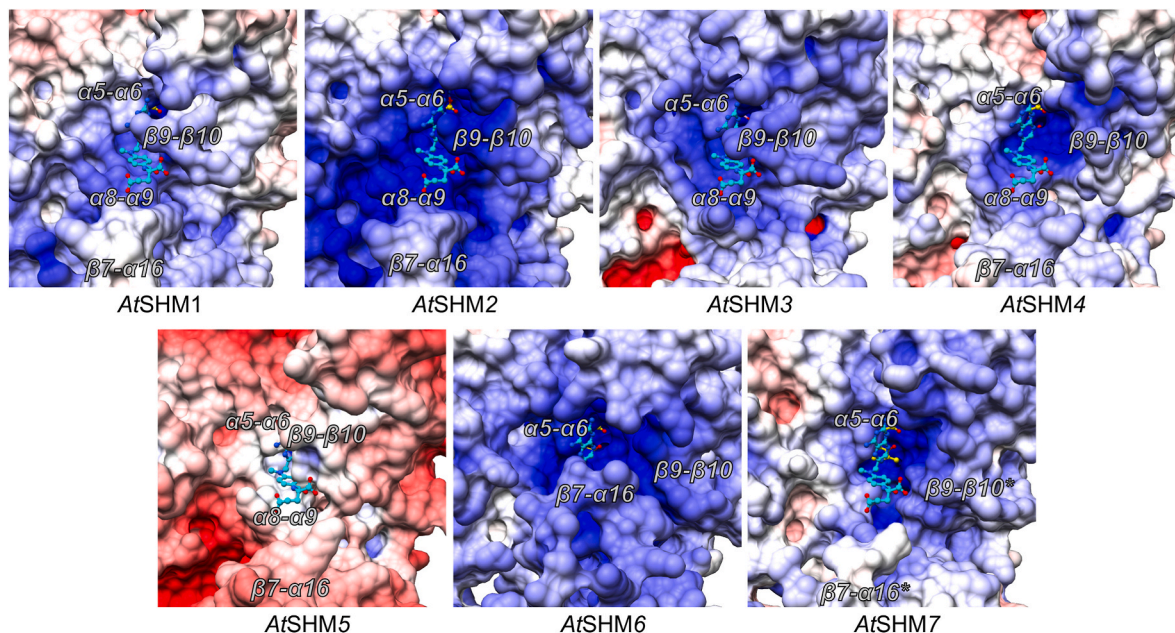


**Fig. 5.** Close-up view of the active site of AtSHM isoenzymes. For the better visualization of the active site, coordinates of methotrexate (cyan ball-and-sticks representation) and PLP-ser external aldimines (yellow), previously published work (Ruszkowski et al., 2019) were superposed with all AtSHMs models. Important regions around the active site discussed in the text are marked. In the last panel showing AtSHM7, asterisk denotes that some residues were not modeled. The view has been rotated along x and y direction of about 15° in comparison to the view shown in Fig. 4.

motif, which, thanks to the positive charge, should be a good binder of the polyglutamylated folates (Fig. 5). In cytosolic AtSHMs, the motif is also positively charged (K-K-G-Q) but it is flanked by proline residues which introduce conformational restrictions. In nuclear AtSHMs, the region responsible for interactions with the polyGlu tails could be K-K-Q-S (AtSHM6) and K-I-R-K-Q (AtSHM7). Additionally, in AtSHM1, there are several lysine residues around the active site, K162, K214, K251, K319, which are not present in AtSHM3. On the other hand, in AtSHM3 contains K214, R215 (this position is occupied by lysine in other isoforms), and K137, which are positioned much closer to the folate binding site. In conclusion, the surface electrostatic potentials vary in the neighborhood of the active site, which apparently determines differences in recognition of THF species with varying Glu<sub>n</sub> lengths.

#### 4. Conclusions and outlook

The reversible reaction of L-serine and THF to glycine and 5,10-CH<sub>2</sub>-THF catalyzed by SHM enzymes provides the major source of one-carbon units for vital metabolic processes (Ser → Gly direction) and is integral for photorespiration (Gly → Ser). Therefore, knowledge of the biochemical properties of each isozyme in the model *A. thaliana* (AtSHM) is essential for understanding and exploiting one-carbon metabolism in plants. The AtSHM5, 6, and 7 isoforms are inactive in both directions of the SHM reaction. Comparison of the structures of all seven AtSHM isoforms suggests that the rationale for inactivity is different for the AtSHM5 isoform and different for AtSHM6-7 (negatively charged surface and hindered PLP binding site in AtSHM5 vs disturbed PLP binding due to substitutions near the presumed PLP site in AtSHM6-7). The same likely applies to other potential biological functions yet to be described, *i.e.*, AtSHM5 may have a different role than AtSHM6-7. Regarding the active (as SHM) isoforms, the high  $k_{cat}$  value for AtSHM1 in the Gly → Ser reaction is in line with its role in photorespiration. In the case of AtSHM3 and AtSHM4, their low  $K_i$  value for THF suggests a role in folate storing. AtSHM4, also shows the lowest  $K_M$  values for substrates in the Ser → Gly reaction and for Gly in the Gly → Ser reaction.

Structures of the AtSHM isoforms reveal significant differences in

regions close to the active site. These fragments surround the entrance to the active site (loop- $\alpha$ 9-loop,  $\beta$ 9- $\beta$ 10 loop and loop- $\alpha$ 25-loop), including that of the neighboring subunit ( $\beta$ 7- $\alpha$ 16 loop). Calculations of the surface electrostatic potentials suggest that variations in those regions may *in vivo* impact the recognition of folate species with different lengths of the Glu<sub>n</sub> tails. The latter is interesting not only in the context of utilizing differentially polyglutamylated THF as substrate but also provides a molecular mechanism for different sensitivity to substrate inhibition in the isoforms. Therefore, multiple SHM isoforms in plants enable autonomous control of SHM activity in the subcellular compartments in addition to participating in photorespiration and providing one-carbon units in the cytosol, nuclei, chloroplast, and mitochondria.

Plant SHM enzymes have been targeted in the herbicide design. Molecules based on the pyrazolopyran scaffold having herbicidal properties are the subject of patent WO 2013/182472A1 2013. The somewhat limited success so far is due to the low metabolic stability of these inhibitors (Schwertz et al., 2017). Considering also the high conservation of SHM active site in higher eukaryotes and therefore difficulties in reaching specificity against plant SHMs, SHM enzymes may not be as promising herbicide targets as previously thought. The potential adverse effects could be harmful to the environment, including humans.

On the other hand, SHM enzymes appear auspicious in the context of providing plant resistance to abiotic and biotic stress. For instance, Moreno et al. (2005) found that defense genes induced by salicylic acid and those involved in H<sub>2</sub>O<sub>2</sub> detoxification were expressed in *Atsh1-1* mutants. This could reflect a response mechanism to ROS accumulation caused by interrupted photorespiration. Mishra et al. examined *Oryza sativa* OsSHM3 in conferring salt stress tolerance by mediating the biosynthetic pathway of glycine to serine interconversion and the synthesis of amino acids (Mishra et al., 2019). Moreover, an SHM gene from Glycine max (SHM8) contributes to soybean cyst nematode (SCN) resistance (Korasick et al., 2020). This recent structural and biochemical characterization of SHM8 isoforms from cultivars Essex and Forrest revealed a dramatic difference in SCN resistance linked to only two amino acid substitutions (Korasick et al., 2020). Hence, exploiting plant SHM in enhancing stress resistance of crops is promising. However, to

make further discoveries, we must seek answers to the following questions regarding plant SHM. What other polymorphisms naturally exist in SHM genes related to plant stress resistance? What is the function of the isoforms that are inactive as SHM enzymes (*AtSHM5-7* in *A. thaliana*)? Are they even enzymes or do they serve purely regulatory purposes?

### Accession numbers

Atomic coordinates and structure factors for the crystal structures have been deposited in the Protein Data Bank (PDB) under the following PDB IDs: *AtSHM2*, 7pzz; *AtSHM4*, 7q00; *AtSHM6*, 7qpe; *AtSHM7*, 7qx8.

### Author statement

IN conceptualized the work and analyzed the expression patterns. IN, SA, AT, and RC performed and analyzed the kinetic experiments. BS solved and refined the structure of SHM7, MR solved and refined the structure of SHM2,4, and 6. MG purified the proteins for SEC analysis and crystalized SHM6. MR, IN, and BS wrote the paper.

### Declaration of competing interest

The authors declare that they have no known competing financial interests or personal relationships that could have appeared to influence the work reported in this paper.

### Data availability

Data will be made available on request.

### Acknowledgments

This work was supported by bilateral cooperative grants from Consiglio Nazionale delle Ricerche (CUP B95F20003020005, to IN) and Polish Academy of Sciences (to MR), and by the Intramural Research Program of the NCI, Center for Cancer Research. Diffraction data were collected at the SER-CAT beamline 22-ID at the Advanced Photon Source, Argonne National Laboratory, supported by the US Department of Energy, Office of Science, Office of Basic Energy Sciences under contract W-31-109-Eng-38 and at beamline P14 operated by EMBL Hamburg at the PETRA III storage ring (DESY, Hamburg, Germany).

### Appendix A. Supplementary data

Supplementary data to this article can be found online at <https://doi.org/10.1016/j.plaphy.2022.07.025>.

### References

- Afonine, P.V., Grosse-Kunstleve, R.W., Echols, N., Headd, J.J., Moriarty, N.W., Mustyakimov, M., Terwilliger, T.C., Urzhumtsev, A., Zwart, P.H., Adams, P.D., 2012. Towards automated crystallographic structure refinement with phenix.refine. *Acta Crystallogr. D* 68, 352–367. <https://doi.org/10.1107/S0907444912001308>.
- Angelaccio, S., Dworkowski, F., Di Bello, A., Milano, T., Capitani, G., Pascarella, S., 2014. Conformational transitions driven by pyridoxal-5'-phosphate uptake in the psychrophilic serine hydroxymethyltransferase from *Psychromonas ingrahamii*. *Proteins* 82, 2831–2841. <https://doi.org/10.1002/prot.24646>.
- Baker, N.A., Sept, D., Joseph, S., Holst, M.J., Mccammon, J.A., 2001. Electrostatics of nanosystems: application to microtubules and the ribosome. *Proc. Natl. Acad. Sci. USA* 98, 10037–10041. <https://doi.org/10.1073/pnas.181342398>.
- Boavida, L.C., Shuai, B., Yu, H.J., Pagnussat, G.C., Sundaresan, V., McCormick, S., 2009. A collection of Ds insertional mutants associated with defects in male gametophyte development and function in *Arabidopsis thaliana*. *Genetics* 181, 1369–1385. <https://doi.org/10.1534/genetics.108.090852>.
- Chitnumsub, P., Ittarat, W., Jaruwat, A., Noytanom, K., Amornwathcharapong, W., Pornthanakasem, W., Chaiyen, P., Yuthavong, Y., Leartsakulpanich, U., 2014a. The structure of *Plasmodium falciparum* serine hydroxymethyltransferase reveals a novel redox switch that regulates its activities. *Acta Crystallogr. D* 70, 1517–1527. <https://doi.org/10.1107/S1399004714005598>.
- Chitnumsub, P., Jaruwat, A., Riangrungraj, P., Ittarat, W., Noytanom, K., Oonanant, W., Vanichthanankul, J., Chuankhayan, P., Maenpuen, S., Chen, C.J., Chaiyen, P., Yuthavong, Y., Leartsakulpanich, U., 2014b. Structures of *Plasmodium vivax* serine hydroxymethyltransferase: implications for ligand-binding specificity and functional control. *Acta Crystallogr. D* 70, 3177–3186. <https://doi.org/10.1107/S1399004714023128>.
- Cruz, E.R., Nguyen, H., Nguyen, T., Wallace, I.S., 2019. Functional analysis tools for post-translational modification: a post-translational modification database for analysis of proteins and metabolic pathways. *Plant J.* 99, 1003–1013. <https://doi.org/10.1111/tpl.14372>.
- Dellero, Y., Mauve, C., Jossier, M., Hodges, M., 2021. The impact of photorespiratory glycolate oxidase activity on *Arabidopsis thaliana* leaf soluble amino acid pool sizes during acclimation to low atmospheric CO<sub>2</sub> concentrations. *Metabolites* 11, 501. <https://doi.org/10.3390/metabo11080501>.
- Dolinsky, T.J., Nielsen, J.E., Mccammon, J.A., Baker, N.A., 2004. PDB2PQR: an automated pipeline for the setup of Poisson-Boltzmann electrostatics calculations. *Nucleic Acids Res.* 32, W665–W667. <https://doi.org/10.1093/nar/gkh381>.
- Emanuelsson, O., Nielsen, H., Brunak, S., Von Heijne, G., 2000. Predicting subcellular localization of proteins based on their N-terminal amino acid sequence. *J. Mol. Biol.* 300, 1005–1016. <https://doi.org/10.1006/jmbi.2000.3903>.
- Emsley, P., Lohkamp, B., Scott, W.G., Cowtan, K., 2010. Features and development of coot. *Acta Crystallogr. D* 66, 486–501. <https://doi.org/10.1107/S0907444910007493>.
- Engel, N., Ewald, R., Gupta, K.J., Zrenner, R., Hagemann, M., Bauwe, H., 2011. The presequence of *Arabidopsis* serine hydroxymethyltransferase SHM2 selectively prevents import into mesophyll mitochondria. *Plant Physiol.* 157, 1711–1720. <https://doi.org/10.1104/pp.111.184564>.
- Fang, C.X., Zhang, P.L., Li, L.L., Yang, L.K., Mu, D., Yan, X., Li, Z., Lin, W.X., 2020a. Serine hydroxymethyltransferase localised in the endoplasmic reticulum plays a role in scavenging H<sub>2</sub>O<sub>2</sub> to enhance rice chilling tolerance. *BMC Plant Biol.* 20. <https://doi.org/10.1186/s12870-020-02446-9>.
- Fang, Y.L., Liu, S.L., Dong, Q.Z., Zhang, K.X., Tian, Z.X., Li, X.Y., Li, W.B., Qi, Z.Y., Wang, Y., Tian, X.C., Song, J., Wang, J.J., Yang, C., Jiang, S.T., Li, W.X., Ning, H.L., 2020b. Linkage analysis and multi-locus genome-wide association studies identify QTNs controlling soybean plant height. *Front. Plant Sci.* 11. <https://doi.org/10.3389/fpls.2020.00009>.
- Gambonnet, B., Jabrin, S., Ravanel, S., Karan, M., Douce, R., Rebeille, F., 2001. Folate distribution during higher plant development. *J. Sci. Food Agric.* 81, 835–841. <https://doi.org/10.1002/jsfa.870>.
- Garrow, T.A., Brenner, A.A., Whitehead, V.M., Chen, X.N., Duncan, R.G., Korenberg, J.R., Shane, B., 1993. Cloning of human cDNAs encoding mitochondrial and cytosolic serine hydroxymethyltransferases and chromosomal localization. *J. Biol. Chem.* 268, 11910–11916.
- Giardina, G., Brunotti, P., Fiascarelli, A., Cicalini, A., Costa, M.G., Buckle, A.M., Di Salvo, M.L., Giorgi, A., Marani, M., Paone, A., Rinaldo, S., Paiardini, A., Contestabile, R., Cutruzzola, F., 2015. How pyridoxal 5'-phosphate differentially regulates human cytosolic and mitochondrial serine hydroxymethyltransferase oligomeric state. *FEBS J.* 282, 1225–1241. <https://doi.org/10.1111/febs.13211>.
- Gout, E., Boisson, A.M., Aubert, S., Douce, R., Bligny, R., 2001. Origin of the cytoplasmic pH changes during anaerobic stress in higher plant cells. Carbon-13 and phosphorus-31 nuclear magnetic resonance studies. *Plant Physiol.* 125, 912–925. <https://doi.org/10.1104/pp.125.2.912>.
- Guiducci, G., Paone, A., Tramonti, A., Giardina, G., Rinaldo, S., Bouzidi, A., Magnifico, M.C., Marani, M., Menendez, J.A., Fatica, A., Maccone, A., Armaos, A., Tartaglia, G.G., Contestabile, R., Paiardini, A., Cutruzzola, F., 2019. The moonlighting RNA-binding activity of cytosolic serine hydroxymethyltransferase contributes to control compartmentalization of serine metabolism. *Nucleic Acids Res.* 47, 4240–4254. <https://doi.org/10.1093/nar/gkz129>.
- Hanson, A.D., Roje, S., 2001. One-carbon metabolism in higher plants. *Annu. Rev. Plant Physiol. Plant Mol. Biol.* 52, 119–137. <https://doi.org/10.1146/annurev.arplant.52.1.119>.
- Hauser, M., Eichelmann, H., Oja, V., Heber, U., Laik, A., 1995. Stimulation by light of rapid pH regulation in the chloroplast stroma in-vivo as indicated by Co<sub>2</sub> solubilization in leaves. *Plant Physiol.* 108, 1059–1066. <https://doi.org/10.1104/pp.108.3.1059>.
- Heldt, H.W., Werdan, K., Milovancev, M., Geller, G., 1973. Alkalization of chloroplast stroma caused by light-dependent proton flux into thylakoid space. *Biochim. Biophys. Acta* 314, 224–241. [https://doi.org/10.1016/0005-2728\(73\)90137-0](https://doi.org/10.1016/0005-2728(73)90137-0).
- Hodges, M., 2002. Enzyme redundancy and the importance of 2-oxoglutarate in plant ammonium assimilation. *J. Exp. Bot.* 53, 905–916. <https://doi.org/10.1093/jxbbot/53.370.905>.
- Huang, X.Y., Chao, D.Y., Koprivova, A., Danku, J., Wirtz, M., Muller, S., Sandoval, F.J., Bauwe, H., Roje, S., Dilkes, B., Hell, R., Kopriva, S., Salt, D.E., 2016. Nuclear localised MORE SULPHUR ACCUMULATION1 epigenetically regulates sulphur homeostasis in *Arabidopsis thaliana*. *PLoS Genet.* 12. <https://doi.org/10.1371/journal.pgen.1006298>.
- Jagath, J.R., Sharma, B., Bhaskar, B., Datta, A., Rao, N.A., Savithri, H.S., 1997. Importance of the amino terminus in maintenance of oligomeric structure of sheep liver cytosolic serine hydroxymethyltransferase. *Eur. J. Biochem.* 247, 372–379. <https://doi.org/10.1111/j.1432-1033.1997.00372.x>.
- Jumper, J., Evans, R., Pritzel, A., Green, T., Figurnov, M., Ronneberger, O., Tunyasuvunakool, K., Bates, R., Zidek, A., Potapenko, A., Bridgland, A., Meyer, C., Kohl, S.A.A., Ballard, A.J., Cowie, A., Romera-Paredes, B., Nikolov, S., Jain, R., Adler, J., Back, T., Petersen, S., Reiman, D., Clancy, E., Zielinski, M., Steinegger, M., Pacholska, M., Berghammer, T., Bodensteiner, S., Silver, D., Vinyals, O., Senior, A.W., Kavukcuoglu, K., Kohli, P., Hassabis, D., 2021. Highly accurate protein structure prediction with AlphaFold. *Nature* 596, 583–589. <https://doi.org/10.1038/s41586-021-03819-2>.

- Kabsch, W., 2010. Xds. *Acta Crystallogr. D* 66, 125–132. <https://doi.org/10.1107/S0907444909047337>.
- Kastanos, E.K., Woldman, Y.Y., Appling, D.R., 1997. Role of mitochondrial and cytoplasmic serine hydroxymethyltransferase isozymes in de novo purine synthesis in *Saccharomyces cerevisiae*. *Biochemistry* 36, 14956–14964. <https://doi.org/10.1021/bi971610n>.
- Keys, A.J., 1999. Biochemistry of photorespiration and the consequences for plant performance. In: Bryant Kruger, N.J., Bryant, J.A., M.M. (Ed.), *Plant Carbohydrate Biochemistry*. BIOS Scientific, Oxford, UK.
- Kim, Y., Babnigg, G., Jedrzejczak, R., Eschenfeldt, W.H., Li, H., Maltseva, N., Hatzos-Skintges, C., Gu, M.Y., Makowska-Grzyska, M., Wu, R.Y., An, H., Chhor, G., Joachimiak, A., 2011. High-throughput protein purification and quality assessment for crystallization. *Methods* 55, 12–28. <https://doi.org/10.1016/j.ymeth.2011.07.010>.
- Korasick, D.A., Kandoth, P.K., Tanner, J.J., Mitchum, M.G., Beamer, L.J., 2020. Impaired folate binding of serine hydroxymethyltransferase 8 from soybean underlies resistance to the soybean cyst nematode. *J. Biol. Chem.* 295, 3708–3718. <https://doi.org/10.1074/jbc.RA119.012256>.
- Kowiel, M., Jaskolski, M., Dauter, Z., 2014. ACHESYM: an algorithm and server for standardized placement of macromolecular models in the unit cell. *Acta Crystallogr. D* 70, 3290–3298. <https://doi.org/10.1107/S1399004714024572>.
- Lakhsassi, N., Patil, G., Piya, S., Zhou, Z., Baharlouei, A., Kassem, M.A., Lightfoot, D.A., Hewezi, T., Barakat, A., Nguyen, H.T., Meksem, K., 2019. Genome reorganization of the GmSHMT gene family in soybean showed a lack of functional redundancy in resistance to soybean cyst nematode. *Sci. Rep.* 9 <https://doi.org/10.1038/s41598-018-37815-w>.
- Li, S., Swanson, S.K., Gogol, M., Florens, L., Washburn, M.P., Workman, J.L., Suganuma, T., 2015. Serine and SAM responsive complex SESAME regulates histone modification crosstalk by sensing cellular metabolism. *Mol. Cell* 60, 408–421. <https://doi.org/10.1016/j.molcel.2015.09.024>.
- Liang, J., Han, Q., Tan, Y., Ding, H., Li, J., 2019. Current advances on structure-function relationships of pyridoxal 5'-phosphate-dependent enzymes. *Front. Mol. Biosci.* 6, 4. <https://doi.org/10.3389/fmolb.2019.00004>.
- Martini, F., Angelaccio, S., Pascarella, S., Barra, D., Bossa, F., Schirch, V., 1987. The primary structure of rabbit liver cytosolic serine hydroxymethyltransferase. *J. Biol. Chem.* 262, 5499–5509.
- Martini, F., Maras, B., Tanci, P., Angelaccio, S., Pascarella, S., Barra, D., Bossa, F., Schirch, V., 1989. The primary structure of rabbit liver mitochondrial serine hydroxymethyltransferase. *J. Biol. Chem.* 264, 8509–8519.
- Matthews, R.G., Drummond, J.T., 1990. Providing one-carbon units for biological methylations - mechanistic studies on serine hydroxymethyltransferase, methylenetetrahydrofolate reductase, and methyltetrahydrofolate-homocysteine methyltransferase. *Chem. Rev.* 90, 1275–1290. <https://doi.org/10.1021/cr00105a010>.
- McClung, C.R., Hsu, M., Painter, J.E., Gagne, J.M., Karlsberg, S.D., Salome, P.A., 2000. Integrated temporal regulation of the photorespiratory pathway. Circadian regulation of two arabidopsis genes encoding serine hydroxymethyltransferase. *Plant Physiol.* 123, 381–391. <https://doi.org/10.1104/pp.123.1.381>.
- McCoy, A.J., Grosse-Kunstleve, R.W., Adams, P.D., Winn, M.D., Storoni, L.C., Read, R.J., 2007. Phaser crystallographic software. *J. Appl. Crystallogr.* 40, 658–674. <https://doi.org/10.1107/S0021889807021206>.
- Mishra, P., Jain, A., Takabe, T., Tanaka, Y., Negi, M., Singh, N., Jain, N., Mishra, V., Maniraj, R., Krishnamurthi, S.L., Sreevathsa, R., Singh, N.K., Rai, V., 2019. Heterologous expression of serine hydroxymethyltransferase-3 from rice confers tolerance to salinity stress in *E-coli* and arabidopsis. *Front. Plant Sci.* 10 <https://doi.org/10.3389/fpls.2019.00217>.
- Moreno, J.I., Martín, R., Castresana, C., 2005. Arabidopsis SHMT1, a serine hydroxymethyltransferase that functions in the photorespiratory pathway influences resistance to biotic and abiotic stress. *Plant J.* 41, 451–463. <https://doi.org/10.1111/j.1365-3113.2004.02311.x>.
- Noctor, G., Arisi, A.C.M., Jouanin, L., Foyer, C.H., 1999. Photorespiratory glycine enhances glutathione accumulation in both the chloroplastic and cytosolic compartments. *J. Exp. Bot.* 50, 1157–1167. <https://doi.org/10.1093/jxb/50.336.1157>.
- Nogués, I., Tramonti, A., Angelaccio, S., Ruskowski, M., Sekula, B., Contestabile, R., 2020. Structural and kinetic properties of serine hydroxymethyltransferase from the halophytic cyanobacterium *Aphanotece halophytica* provide a rationale for salt tolerance. *Int. J. Biol. Macromol.* 159, 517–529. <https://doi.org/10.1016/j.ijbiomac.2020.05.081>.
- Pagnussat, G.C., Yu, H.J., Ngo, Q.A., Rajani, S., Mayalagu, S., Johnson, C.S., Capron, A., Xie, L.F., Ye, D., Sundaresan, V., 2005. Genetic and molecular identification of genes required for female gametophyte development and function in Arabidopsis. *Development* 132, 603–614. <https://doi.org/10.1242/dev.01595>.
- Peterson, E.A., Sober, H.A., 1954. Preparation of crystalline phosphorylated derivatives of vitamin-B6. *JACS* 76, 169–175. <https://doi.org/10.1021/ja01630a045>.
- Reed, M.C., Lieb, A., Nijhout, H.F., 2010. The biological significance of substrate inhibition: a mechanism with diverse functions. *Bioessays* 32, 422–429. <https://doi.org/10.1002/bies.200900167>.
- Reid, K.S.C., Lindley, P.F., Thornton, J.M., 1985. Sulfur-aromatic interactions in proteins. *FEBS (Fed. Eur. Biochem. Soc.) Lett.* 190, 209–213. [https://doi.org/10.1016/0014-5793\(85\)81285-0](https://doi.org/10.1016/0014-5793(85)81285-0).
- Renwick, S.B., Snell, K., Baumann, U., 1998. The crystal structure of human cytosolic serine hydroxymethyltransferase: a target for cancer chemotherapy. *Structure* 6, 1105–1116.
- Ruskowski, M., Sekula, B., Ruskowska, A., Contestabile, R., Nogués, I., Angelaccio, S., Szczepaniak, A., Dauter, Z., 2019. Structural basis of methotrexate and pemetrexed action on serine hydroxymethyltransferases revealed using plant models. *Sci. Rep.* 9, 19614 <https://doi.org/10.1038/s41598-019-56043-4>.
- Ruskowski, M., Sekula, B., Ruskowska, A., Dauter, Z., 2018. Chloroplastic serine hydroxymethyltransferase from *Medicago truncatula*: a structural characterization. *Front. Plant Sci.* 9, 584. <https://doi.org/10.3389/fpls.2018.00584>.
- Scarsdale, J.N., Kazanina, G., Radaev, S., Schirch, V., Wright, H.T., 1999. Crystal structure of rabbit cytosolic serine hydroxymethyltransferase at 2.8 Å resolution: mechanistic implications. *Biochemistry* 38, 8347–8358. <https://doi.org/10.1021/bi9904151>.
- Scarsdale, J.N., Radaev, S., Kazanina, G., Schirch, V., Wright, H.T., 2000. Crystal structure at 2.4 Å resolution of *E. coli* serine hydroxymethyltransferase in complex with glycine substrate and 5-formyl tetrahydrofolate. *J. Mol. Biol.* 296, 155–168. <https://doi.org/10.1006/jmbi.1999.3453>.
- Schirch, L., 1982. Serine hydroxymethyltransferase. *Adv. Enzymol. Relat. Area Mol. Biol.* 53, 83–112.
- Schirch, V., Szebenyi, D.M.E., 2005. Serine hydroxymethyltransferase revisited. *Curr. Opin. Chem. Biol.* 9, 482–487. <https://doi.org/10.1016/j.cbpa.2005.08.017>.
- Schwartz, G., Witschel, M.C., Rottmann, M., Bonner, R., Leartsakulpanich, U., Chitnumsub, P., Jaruwat, A., Ittarat, W., Schafer, A., Aponte, R.A., Charman, S.A., White, K.L., Kundu, A., Sadhulhan, S., Lloyd, M., Freiberg, G.M., Srikumaran, M., Siggel, M., Zwyssig, A., Chaiyen, P., Diederich, F., 2017. Antimalarial inhibitors targeting serine hydroxymethyltransferase (SHMT) with in vivo efficacy and analysis of their binding mode based on X-ray cocrystal structures. *J. Med. Chem.* 60, 4840–4860. <https://doi.org/10.1021/acs.jmedchem.7b00008>.
- Shen, J., Zeng, Y., Zhuang, X., Sun, L., Yao, X., Pimpl, P., Jiang, L., 2013. Organelle pH in the arabidopsis endomembrane system. *Mol. Plant* 6, 1419–1437. <https://doi.org/10.1093/mp/ss079>.
- Sipari, N., Lihavainen, J., Shapiguzov, A., Kangasjarvi, J., Keinänen, M., 2020. Primary metabolite responses to oxidative stress in early-senescing and paraquat resistant Arabidopsis thaliana rcd1 (Radical-Induced cell Death1). *Front. Plant Sci.* 11, 194. <https://doi.org/10.3389/fpls.2020.00194>.
- Somerville, C.R., Ogren, W.L., 1981. Photorespiration-Deficient mutants of arabidopsis-thaliana lacking mitochondrial serine transhydroxymethylase activity. *Plant Physiol.* 67, 666–671. <https://doi.org/10.1104/pp.67.4.666>.
- Szebenyi, D.M., Liu, X., Kriksunov, I.A., Stover, P.J., Thiel, D.J., 2000. Structure of a murine cytoplasmic serine hydroxymethyltransferase quinonoid ternary complex: evidence for asymmetric obligate dimers. *Biochemistry* 39, 13313–13323. <https://doi.org/10.1021/bi000635a>.
- Terwilliger, T.C., Grosse-Kunstleve, R.W., Afonine, P.V., Moriarty, N.W., Zwart, P.H., Hung, L.W., Read, R.J., Adams, P.D., 2008. Iterative model building, structure refinement and density modification with the PHENIX AutoBuild wizard. *Acta Crystallogr. D* 64, 61–69. <https://doi.org/10.1107/S090744490705024X>.
- Timm, S., Hagemann, M., 2020. Photorespiration-how is it regulated and how does it regulate overall plant metabolism? *J. Exp. Bot.* 71, 3955–3965. <https://doi.org/10.1093/jxb/eraa183>.
- Toufighi, K., Brady, S.M., Austin, R., Ly, E., Provart, N.J., 2005. The botany array resource: e-northers, expression angling, and promoter analyses. *Plant J.* 43, 153–163. <https://doi.org/10.1111/j.1365-3113.2005.02437.x>.
- Tramonti, A., Paiardini, A., Paone, A., Bouzidi, A., Giardina, G., Guiducci, G., Magnifico, M.C., Rinaldo, S., Mcdermott, L., Menendez, J.A., Contestabile, R., Cutruzzola, F., 2018. Differential inhibitory effect of a pyrazolopyran compound on human serine hydroxymethyltransferase-amino acid complexes. *Arch. Biochem. Biophys.* 653, 71–79. <https://doi.org/10.1016/j.abb.2018.07.001>.
- Voll, L.M., Jamai, A., Renne, P., Voll, H., McClung, C.R., Weber, A.P.M., 2006. The photorespiratory Arabidopsis shm1 mutant is deficient in SHM1. *Plant Physiol.* 140, 59–66. <https://doi.org/10.1104/pp.105.071399>.
- Wang, D.K., Liu, H.Q., Li, S.J., Zhai, G.W., Shao, J.F., Tao, Y.Z., 2015. Characterization and molecular cloning of a serine hydroxymethyltransferase 1 (OsSHM1) in rice. *J. Integr. Plant Biol.* 57, 745–756. <https://doi.org/10.1111/jipb.12336>.
- Wei, Z., Sun, K., Sandoval, F.J., Cross, J.M., Gordon, C., Kang, C., Roje, S., 2013. Folate polyglutamylation eliminates dependence of activity on enzyme concentration in mitochondrial serine hydroxymethyltransferases from Arabidopsis thaliana. *Arch. Biochem. Biophys.* 536, 87–96. <https://doi.org/10.1016/j.abb.2013.06.004>.
- Willems, P., Horne, A., Van Parys, T., Goormachtig, S., De Smet, I., Botzki, A., Van Breusegem, F., Gevaert, K., 2019. The Plant PTM Viewer, a central resource for exploring plant protein modifications. *Plant J.* 99, 752–762. <https://doi.org/10.1111/tpj.14345>.
- Winter, D., Vinegar, B., Nahal, H., Ammar, R., Wilson, G.V., Provart, N.J., 2007. An "Electronic Fluorescent Pictograph" browser for exploring and analyzing large-scale biological data sets. *PLoS One* 2, e718. <https://doi.org/10.1371/journal.pone.0000718>.
- Zhang, Y., Sun, K.H., Sandoval, F.J., Santiago, K., Roje, S., 2010. One-carbon metabolism in plants: characterization of a plastid serine hydroxymethyltransferase. *Biochem. J.* 430, 97–105. <https://doi.org/10.1042/Bj20100566>.
- Zhang, Y.H., Dai, L., Liu, Y., Zhang, Y.H., Wang, S.P., 2017. Identifying novel fruit-related genes in Arabidopsis thaliana based on the random walk with restart algorithm. *PLoS One* 12. <https://doi.org/10.1371/journal.pone.0177017>.
- Zhu, H.Y., Kim, D.J., Baek, J.M., Choi, H.K., Ellis, L.C., Kuester, H., McCombie, W.R., Peng, H.M., Cook, D.R., 2003. Syntenic relationships between *Medicago truncatula* and Arabidopsis reveal extensive divergence of genome organization. *Plant Physiol.* 131, 1018–1026. <https://doi.org/10.1104/pp.102.016436>.